MPhil/PhD Transfer Report

Coherent X-ray diffraction Imaging and Bragg-geometry Ptychography studies on Silicon-On-Insulator Nanostructures

Xiaowen Shi

Department of Physics and Astronomy & London Centre for Nanotechnology
University College London
U.K.

Supervisor: **Prof. Ian Robinson** (UCL Department of Physics and Astronomy & London Centre for Nanotechnology)

Second Supervisor: **Dr. Paul Warburton** (UCL Department of Electrical Engineering & London Centre for Nanotechnology)

Table of Contents

Abstract

My initial objective of my PhD project is on coherent X-ray diffractive imaging (CDI) techniques to study strained Silicon-On-Insulator (SOI) and Strained-Silicon-On-Insulator (SSOI) nanostructures, which include nanowires and micro-squares. To understand and distinguish SOI wafer properties and compare and analyze difference wafer bonding techniques, various SOI wafers with different bonding techniques were measured by using CDI, and analysis shows inhomogeneity across all categories of SOI wafers. Furthermore, it is noted that discovered that radiation-bending effect causes Silicon-On-Insulator nanowires to exhibit highly strained characteristics in diffraction patterns in reciprocal-space. There is a trend of peak splitting of maximum frames of diffraction patterns when increasing X-ray illumination dose, i.e. time of X-ray exposure. We are able to propose a model of radiation-induced bending of SOI model and our model is confirmed by simulations of calculated diffraction patterns and by Finite-Element-Analysis calculations tool (COMSOL Multiphysics). The result is in excellent agreement with experimental measurements, which strongly indicate that our model is correct for illustration of radiation effect. Our newly-invented Revised Hybrid-Input-Output algorithm is introduced and our simulations show improvement of reconstructions of highly complex direct-space objects comparing with conventional CDI algorithms. Reconstructions of real diffraction data of SOI nanowires with highy-strained features (due to radiation-induced bending) to be directed by calculated models are under development to be reported in the near future. In the second half of my PhD project, I will be concentrating on development of reflection Bragg-geometry ptychography at beamline 34-ID-C at the Advanced Photon Source. We propose zone-plate focused method that would generate highly asymmetric curved-wave front probe illumination for Bragg-geometry ptychography studies on SOI micro- and nano squares and most importantly, the various SOI and SSOI wafers that are fabricated with different techniques. Bragg-geometry ptychography has great potential in condensed matter structures and surface sciences aiming at better understanding of structural Physics, Materials sciences and Nanotechnology in general. We propose to study three-dimensional atomic displacement fields caused by this effect in SOI based devices in the near future by both conventional Bragg CDI and Bragg-geometry ptychography. The last part of my project involves preparation and possibly preliminary studies of strain evolutions of SOI based MOSFET devices under device operating conditions by using CDI. Our experimental results along with supporting theory suggest that Silicon-On-Insulator MOSFET technology might be sensitive to radiation and its related effects, the resulting devices performance upon radiation effect can be very important to semiconductor industry.

1 Coherence of X-ray Science and applications

1.1 Introduction to Coherent X-ray Diffractive Imaging

Coherent X-ray Diffractive Imaging (CDI)[1-6], especially using phase-contrast, is one of the strongest contenders for investigating internal structures (both atomic density and phases) of nano-crystalline materials. More conventional imaging techniques such as Transmission Electron Microscopy (TEM) can only probe very thin cross-sections of the specimen under study[7]. Any internal stresses could possibly be removed when samples are cross-sectioned to produce thin lamellar sections. On the contrary, with CDI, we can probe the 3-dimensional internal structure of entire samples without damaging samples structures into very thin slices so that they can be imaged by high-resolution electron microscope.

The Coherent X-ray diffractive imaging technique has better reconstructed real-space resolution, presently around 30nm, than direct real-space imaging X-ray methods because of the inversion procedure used for the reciprocal-space diffraction patterns. To be able to image structures in reciprocal-space, coherent diffractive imaging, in both hard X-ray and visible light, is expected to offer much better, at least a factor of three better than spatial resolution (theoretically it can reach atomic resolution) than its traditional X-ray imaging counterpart such as Transmission X-ray Microscopy[8, 9]. Bragg CDI is able to investigate strains, seen as atomic displacements (from the ideal atomic position in a crystal lattice) of blocks of material with dimensions of 10nm to 1μm. It allows measurements of strains of individual regions while most diffraction techniques obtain results by averaging arrays of similar structures[10].

We were able to visualize large strains in single isolated Silicon nanowires with the help of a confocal microscope installed at beamline 34-ID-C at the Advanced Photon Source. The measurements were taken at X-ray of energy of 8.9keV (with Si (111) channel-cut single-crystalline monochromator) with both horizontal and vertical KB mirrors as focusing optics. Roller-slits were used to preserve incoming coherence and quality of X-ray spectrum, the horizontal and vertical slits were set to be 50 and 20 μm respectively, though slits widths can be adjusted depending coherence properties of incoming X-ray beam and the setups properties of the upstream mirror during experiments. Three-dimensional rocking curves are measured

at a particular Bragg reflection of Silicon by rocking specimen around ±0.5 degree with incidence angle of around 0.5 to 10 degree. The angle of incidence can be optimized depending on the spacing between adjacent Silicon nanostructures and experimental purposes. Generally, higher incidence angles result to smaller X-ray beam footprints, which in term reduce the scattering and interference effects of two or multiple Silicon nanostructures under X-ray beam illumination volume, if that is more desirable for measurements. Also, if the nanostructures to be measured are composed of the same materials and have the same crystal orientations, signal-to-noise (STN) should be maximized to ensure good quality of diffraction data. To achieve this, it was recently discovered that with higher incidence angle, the substrate-related Crystal Truncation Rod (CTR) contribution to the diffraction intensity, which is usually undesirable, could be substantially decreased, due to reduced substrate illumination area on substrates of X-ray beam resulting to less CTR signals in diffraction data. As a result, the Signal-to-Noise-Ratio (SNR) could be improved leading to better data reconstructions in analysis.

Imaginary part of the exit wave-function of specimen contributes to phases or displacements of direct-space wave-field, where the real-part of the wave-function gives rise to electronic density of direct-space wave-field. Discrete Fourier Transform of complex wave-functions of asymmetrical amplitudes or phases will generate asymmetric diffraction patterns in reciprocal-space. On the contrary, diffraction patterns of real objects (amplitude only with no phases) will be symmetric; this is fully explained by the Friedel law[11] and Fourier Transform Theorem. Furthermore, Our simulation shows that objects with symmetric structures for both amplitude and phase, will also have symmetric diffraction intensities, regardless the complexity of the phase structures of objects. Therefore, in order to generate highly asymmetric diffraction patterns, one has to make sure the direct-space phases of object are highly asymmetric.

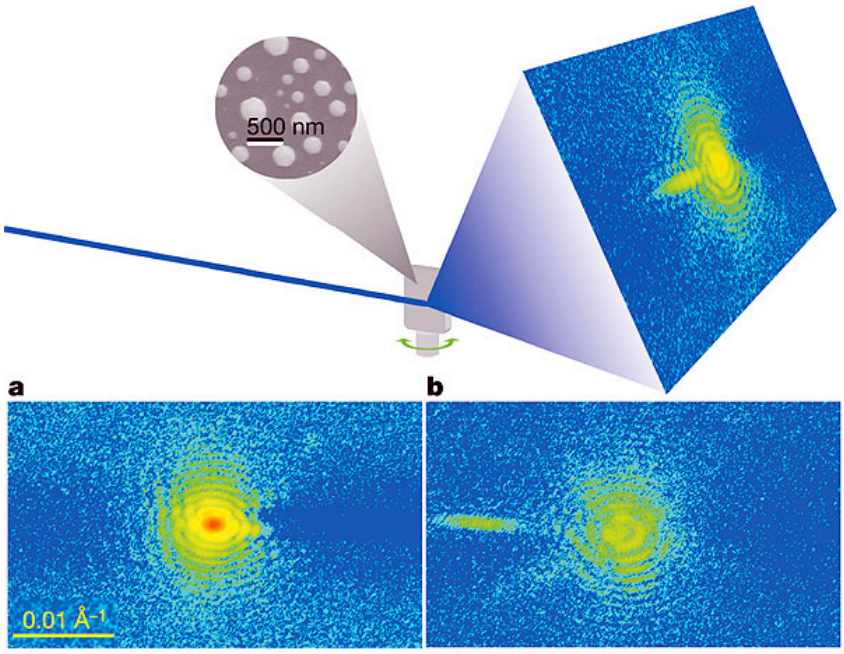

Fig. 1 Pb was evaporated onto a heated Si wafer support, with its native oxide intact, to make a film of about 20 nm thickness. After melting the film, it formed molten droplets, which were then cooled to overcome the (substantial) supercooling until the liquid crystallized, then raised again to 1.2 K below the Pb melting point of 600.6 K. Ultrahigh vacuum conditions were maintained throughout. Later examination by SEM (circular inset) showed isolated hemispherical crystals. Undulator X-rays from the Advanced Photon Source (APS) were monochromated using Si(111), selecting a wavelength of 1.38 Å, and collimated by narrow slits to illuminate a few hundred crystals of the sample. A direct-reading CCD X-ray detector, 1.32 m away, was centred on the (111) Bragg peak of one of the crystals, to give the diffraction patterns shown. A rotation series of 50 diffraction patterns was collected by rotating the sample in steps of 0.01° about the axis shown. Two representative frames are shown in **a** and **b**, while a fuller series is given in Supplementary Fig. S2. The total exposure time of each frame was 150 s. Figure is from[12]

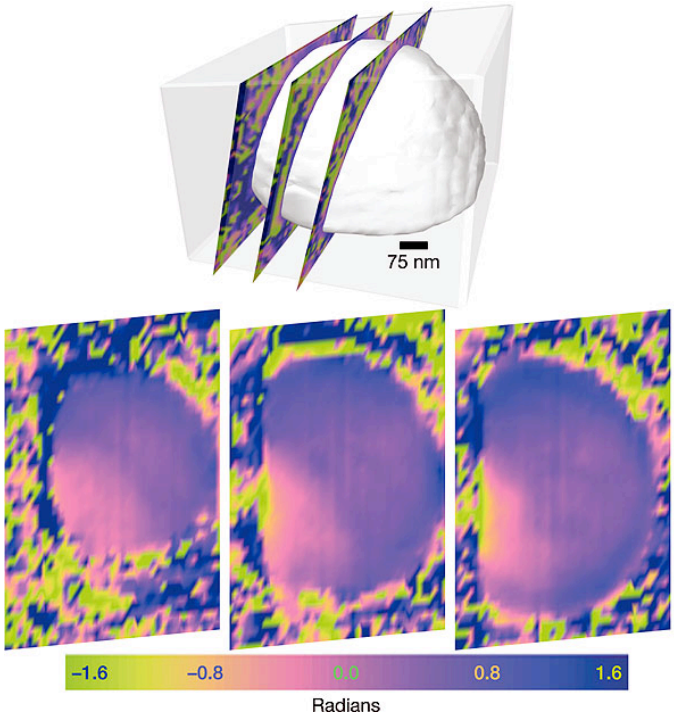

Fig. 2 Schematic diagram of the sections, 138 nm apart. The translucent box is the support region used in the phasing calculations, which was rectangular before the coordinate transformation. The phase bulge is interpreted as a projection of strain fields in the crystal lattice arising from contact forces at the interface with the substrate. Figure is from[12]

1:2 Coherent Properties of X-ray of 3rd and 4th Generation Sources

Conventional X-ray with low degree of coherence is used to study specimen of highly crystalline structures, with introduction of X-ray studies with high coherence properties, specimen with non-crystalline or semi-crystalline kind can be also studied because of the coherence properties of incident X-ray produce interference patterns to be recorded as speckles and these patterns could in principle be inverted if necessary data acquisition and experimental conditions are to be met.

Coherence function of X-ray can be regarded to be a multi-dimensional entity, with longitudinal and transverse coherence lengths defined as follows:

$$\xi_L = \frac{\lambda^2}{2\Delta\lambda}$$ [13]

$$\xi_T = \frac{\lambda R}{2\sigma_{x,y}}$$ [13]

Where λ is the wavelength of incident X-ray and Δλ is the difference in wavelength between different incident waves, and $\sigma_{x,y}$ is the finite source sizes of accelerated electrons from which X-ray is produced, R being the distance the incident X-ray travels and it is considered that $R \gg \sigma_{x,y}$, and it is the distance between sample and X-ray detector. Coherence length is regarded as the length at which two incident X-ray waves are just completely out of phase, i.e. out-of-phase by $\frac{\pi}{2}$. Longitudinal and transverse coherence lengths were measured to be $\xi_L = 0.66 \pm 0.22\,\mu$m [14], but the transverse coherence length is significantly longer and it is estimated to be around 50 to 100μm at beamline 34-ID-C at the Advanced Photon Source (APS). Mutual coherence function (MCF) is generally defined as:

$$\Gamma(\rho_1, \rho_2, \tau) = \langle \mathrm{E}(\rho_1, t)\mathrm{E}^*(\rho_2, t+\tau) \rangle$$

And the normalized mutual coherence function is usually described as the follows;

$$\gamma(\rho_1, \rho_2, \tau) = \frac{\langle \mathrm{E}(\rho_1, t)\mathrm{E}^*(\rho_2, t+\tau) \rangle}{\sqrt{\langle \mathrm{I}(\rho_1, t) \rangle \langle \mathrm{I}(\rho_2, t) \rangle}}$$

ρ_1 and ρ_2 are position vectors of two points at a particular wave front in which two points are located. $\mathrm{E}(\rho_1, t)$ and $\mathrm{E}^*(\rho_2, t+\tau)$ are electromagnetic fields at these two points which are separated by a specific time interval of τ, after some time t in the initial starting point of measurement. $\langle \mathrm{I}(\rho_1, t) \rangle$ and $\langle \mathrm{I}(\rho_2, t) \rangle$ are expectation values of intensity of electromagnetic field at these two points in the wave front. The value $\gamma(\rho_1, \rho_2, \tau)$ can be between 0 and 1,

with value of 0 being complete incoherence and being 1 being complete coherence, which means any values of $\gamma(\rho_1, \rho_2, \tau)$ being between 0 and 1 indicate that the X-ray source is partially coherent. With definition of mutual coherence function (MCF), one can calculate electromagnetic field strength at the second point at a particular wave front in the incoming X-ray source whenever the illumination is fully coherent, and in contrast, no information can be deduced on the electromagnetic field strength of the second point if the source is completely incoherent ($\gamma(\rho_1, \rho_2, \tau)$ is 0).

Recent review has indicated that coherence properties of X-ray cannot be compared with that of visible light, i.e. laser, therefore limited coherence length results to partial coherence measurements and the possible effect of partial coherence properties to CDI measurements[15]. By taking partial coherence effects into account, CDI reconstructions of gold nano-crystals can be improved by using approximate three-dimensional structures of X-ray probe function. Multi-dimensional coherent functions of X-rays[16] in a sense indicate that there is somewhat coherent property in all three spatial dimensions, i.e. there is an extra coherence length in the 3rd dimension, which is differ from its longitudinal and transverse parts of coherence dimensions. However, it is yet to be demonstrated with experimental measurements to determine this extra dimension of the coherence function. One clever way to measure coherence function of X-ray is the Young's double-slit experiment with measurements of visibility of fringes in reciprocal-space as a function of slit separation, recent results shows such measurements by using hard X-ray free electron laser at Linac Coherent Light Source (LCLS) at Stanford[17]. The estimation of coherence length comes from approximation of slit separation distance once the visibility of fringes in measured diffraction patterns reduced to a standard value of e^{-1} of that of full visibility level with total coherence.

1:3 Coherence and Bragg's Law of X-ray Diffraction of Finite Crystals

A finite crystal structure is composed with crystal lattice system and the type of unit cell. Unit

cell is defined as a group of atoms in such an arrangement that has strong association with lattice points in crystal structure. Atoms in a specific unit cell structure have special orientations to that lattice points in a specific crystal structure[18].

Amplitude function of a finite crystal can be derived to have the form of convolution of unit cell function of the crystal structure with the product of function of infinite lattice and crystal shape function.

$$f(\text{Finite Crystal}) = f(\text{Unit Cell}) \otimes [f(\text{Infinite Lattice}) \times f(\text{Shape Function})]$$

Where the crystal shape function can be either real or complex.

Consequently the Fourier Transform of the finite crystal function can be derived to be product of Fourier Transform of unit cell function of the crystal structure to the convolution of Fourier Transform of infinite lattice function with the Fourier Transform of crystal shape function, which can be expressed as follows;

$$FT\{f(\text{Finite Crystal})\} = FT\{f(\text{Unit Cell})\} \times [FT\{f(\text{Infinite Lattice})\} \otimes FT\{f(\text{Shape Function})\}]$$

Where FT indicates Fourier Transform operation.

Bragg's law of X-ray diffraction states that incoming coherent X-ray scatters with atoms in lattice planes of unit cells of crystal specimen with lattice planes indicated by miller indices of $\{h,k,l\}$ can result to either constructive or destructive interference patterns if and only if the path length differences of the X-ray waves are of integers multiple of wavelength of the incoming X-ray, with the angle between different lattice planes with $\{h,k,l\}$ index is the Bragg angle θ, which can be described as the follows:

$$2d \times \text{Sin}(\theta) = n \times \lambda$$

In order to fulfill Bragg condition of X-ray scattering, the wavelength of incoming X-ray has to be comparable to that of the lattice parameters of the crystal specimen. As a result, depending on crystal structures and lattice parameters of various crystals, the energy of X-ray could be carefully calibrated to obtain appropriate Bragg diffraction peaks.

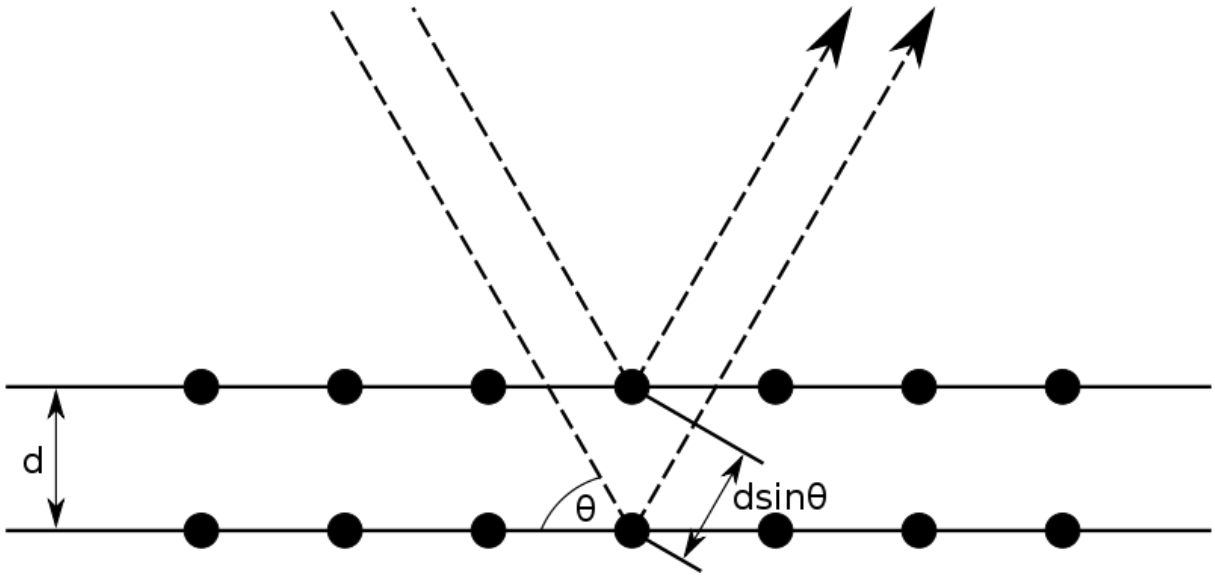

Fig. 3 illustration of Bragg's law. image comes from online Wikipedia:
http://en.wikipedia.org/wiki/Bragg%27s_law

When atoms in the finite crystal lattices deviate from their ideal positions or defects/impurities are present in the crystals, both of which could generate displacements fields inside finite crystals. The displacements can be converted into phases by calculating their scalar product of reciprocal-space vector Q of specific Bragg diffraction peak to the displacements fields along the Q direction. The magnitude of Q is calculated by 2π dividing the crystal lattice constant of specific Bragg peak. The derivation of the direct-space displacements and phase relationship has been addressed in details by Robinson et al[2]. The red lines indicated in Fig. 4 correspond to the total phase shifts of incoming X-ray relative to that of the crystal specimen, which can be calculated by $\vec{k}_f \bullet \vec{u} - \vec{k}_i \bullet \vec{u} = \vec{Q} \bullet \vec{u}$. Therefore, phases shifts of Bragg scattering at specific Bragg condition with reciprocal-space vector Q can be evaluated in this way, and this results to complex direct-space object shape function. When object shape functions are complex, the corresponding diffraction patterns will be

asymmetric.

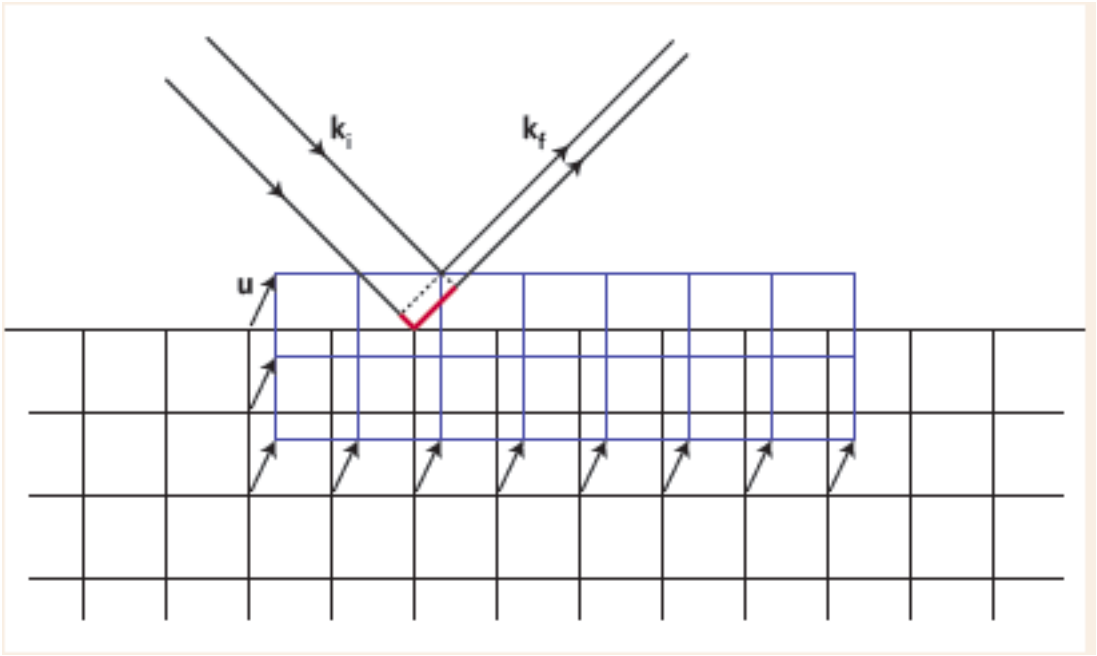

Fig 4 Image from Ref[19]

$$\tilde{\rho}(\mathrm{r}) = \rho(\mathrm{r})e^{i\Phi}$$

Where $\tilde{\rho}(\mathrm{r})$ is the complex crystal shape function and Φ is the phase.

The information obtained with X-ray diffraction can be used to evaluate shape function of crystals, both real and complex, from experimental diffraction intensity, which is squared modulus of Fourier Transform of scattered exit wave function of Bragg diffraction.

X-ray Scattering process can be elastic or inelastic, or a combination of these. In general, elastic scattering, which is also called Thomson scattering of single electrons have a total cross-section described as follows:

$$\sigma_{\text{electron}} = 8\pi r_e^2 / 3 = 6.652 \times 10^{-29}\ \text{m}^2$$ [20]

Where r_e is the classical radius of an electron.

Scattering from atoms can be considered to be scattering of aggregate of electrons in atoms, which is a cooperative procedure of scattering, and the cross-section can be generalized as follows:

$$\sigma_{\text{atom}} = 8\pi r_e^2 \int_{-1}^{1} \left| f(\theta) \right|^2 (1+\cos^2\theta)\, d(\cos\theta)$$ [21]

Where θ is the scattering angle, and $f(\theta)$ is the complex atomic scattering factor, it is approximately independent scattering angles, and has its real part representing the effective density of scatters or scattering probability within atoms of particular kinds.

The total scattering length of an atom can be expressed as:

$$-\mathrm{r}_0 f^0(\mathrm{Q}) = -\mathrm{r}_0 \int \rho(\mathrm{r}) \exp(i\mathrm{Q}.\mathrm{r}).\mathrm{dr}$$ [22]

Where $f^0(\mathrm{Q})$ is the atomic form factor and r_0 is the Thomson scattering length.

Detailed descriptions of diffraction by a three-dimensional lattice in crystal samples are illustrated in Ref [6], where W.L. Bragg's theorem of Bragg X-ray diffraction of lattice planes within crystals are discussed. To extend Bragg diffraction to three-dimensional structures from 1D or 2D is not straightforward, the diffraction patterns obtained mainly by X-ray diffraction of electrons within crystal samples, and several important factors for obtaining three-dimensional diffraction patterns. Two-dimensional infinite crystal is composed with a set of atomic positions, i.e. the delta-functions convoluting with electron density function for a single atom. Infinity numbers of unit cells, within which atomic positions function repeats would lead to the definition of infinite crystals. To study a finite three-dimensional crystal sample, one needs to multiple the infinite crystal function by a three-dimensional shape function, in which all the external boundaries are appropriately defined. This

leads to X-ray diffraction of finite crystal samples[23].

Scattering of finite crystals can be evaluated by Born-Oppenheimer approximation, the details of derivation and analysis was reported by C. Scheringer [24][25] , from which we could extend scattering of finite crystals, and the complex scattered exit wave function can be described as follows:

$$\tilde{A} = FT\{\rho(r)e^{i\Phi} \times S \times f(r)\, dV\}$$

Where $\rho(r)e^{i\Phi}$ is the complex electronic density of crystal specimen, with Φ representing phases, S is the proportionality constant, and $f(r)$ is the density of scatters within volume dV with three-dimensional position vector r.

The measured intensity of diffraction patterns in experiments can be evaluated as Modulus Square of complex scattered exit wave function as follows:

$$I = \left| \tilde{A} \right|^2$$

There are a number of mathematical symmetries associated with Fourier Transform.

(1) Symmetry of shift of origin in x

When a function is to be translated along a particular axis, the Fourier Transform of the function will only differ from that of its un-translated one in phases, while the amplitude of its Fourier Transform result is the same. This can be derived as follows:

$$\mathrm{F_1(q)}=\int_{-\infty}^{\infty} f(x-x_0)\exp(-iqx)dx=\int_{-\infty}^{\infty} f(x')\exp[-iq(x'+x_0)]dx'=\exp(-iqx_0)\int_{-\infty}^{\infty} f(x')\exp(-iqx')\,dx'=\exp(-iqx_0)\,F(\mathrm{q})$$

[6]

Which states that Fourier Transform of $f(x-x_0)$ only differs to that of original function $f(x)$ with phase factor $\exp(-iqx_0)$.

(2) Symmetry of shift of origin in q

When a function is to be translated in q, symmetry property of its Fourier Transform holds as follows:

$$\mathrm{F_1}(x)=\int_{-\infty}^{\infty} f(\mathrm{q}-\mathrm{q_0})\exp(-i(\mathrm{q})x)d\mathrm{q}=\int_{-\infty}^{\infty} f(\mathrm{q}')\exp(-iq'x)\exp(-iq_0x)d\mathrm{q}'=\exp(-iq_0x)\int_{-\infty}^{\infty} f(\mathrm{q}')\exp(-ik\mathrm{q}')\,d\mathrm{q}'=\exp(-iq_0x)\,\mathrm{F}(x)$$

The difference between $\mathrm{F_1}(x)$ and $\mathrm{F}(x)$ is also a phase factor, in this case $\exp(-iq_0x)$. It can be seen that the symmetry of shift of origin holds for Fourier Transform from direct-space to reciprocal-space and the opposite direction is also true.

(3) Inverse of Fourier Transform

The inversion symmetry states that the Inverse Fourier Transform of the Fourier Transform of a function is the function itself provided $\int_{-\infty}^{\infty}|f(x)|dx$ is finite.

$$\mathrm{FT(q)}=\int_{-\infty}^{\infty} f(x)\exp(-iqx)dx$$

$$f(x)=\frac{1}{2\pi}\int_{-\infty}^{\infty}\mathrm{FT(q)}\exp(i\mathrm{qx})\mathrm{dq}$$

Where FT (q) indicates Fourier Transform operation.

Discrete Fourier Transform can be calculated as follows:

$$\mathrm{DFT(q)}=\sum_{\mathrm{n=0}}^{\mathrm{N\text{-}1}}\rho(\mathrm{r})_{\mathrm{n}}.\exp(-i2\pi\frac{\mathrm{q}}{\mathrm{N}}\mathrm{n})$$

Where N is the number of pixels in dataset arrays, DFT method is used for Fourier Transform calculations of finite-size arrays.

(4) Inversion Symmetries of Fourier Transform

The inversion symmetry states that if a function $f(x)$ is centro-symmetric, $f(x)=f(-x)$, then the Fourier Transform of the function is also centro-symmetric, $\mathrm{FT(q)}[f(x)]=\mathrm{FT}(-\mathrm{q})[f(x)]$. On the contrary, if a function $f(x)$ is anti-centro-symmetric, $f(x)=-f(-x)$, then the Fourier Transform of the function is also anti-centro-symmetric, $\mathrm{FT(q)}[f(x)]=-\mathrm{FT}(-\mathrm{q})[f(x)]$.

(5) Friedel's law and beyond

Following Inversion symmetries of Fourier Transform, Friedel's law states that if a direct-space object function is real, then its amplitude of Fourier Transform is symmetric. In other words, if a direct-space object function is complex, asymmetric Fourier Transform

amplitude will be produced. In addition to these, our simulations show that the amplitude of Fourier Transform of a complex direct-space object function is asymmetric only and only if the phases in the direct-space complex object function are asymmetric, otherwise, symmetric phases in the object function will result to symmetric amplitude of its corresponding Fourier Transform.

2 Algorithms of Coherent Diffraction Imaging (CDI) in Bragg Geometry

2:1 well-developed algorithms in Coherent X-ray diffraction imaging (CDI)

Many algorithms are associated with reconstructions of CDI measured data, such as Error reduction; Hybrid-Input-Output and Phase-Constraint Hybrid-Input-Output. Other useful algorithms are also widely used such as difference map, which is a generalized form for Hybrid-Input-Output algorithm and shrink-wrap, which is extremely useful for compact nano-crystals, such as Gold nano-crystals. Recent developments on highly strained compact objects have demonstrated significant improvements[10, 26, 27], and combinations of several different algorithms have also been demonstrated to show better results in some cases[26]. However, none of the existing algorithms or combinations of these could in principle guarantee convergence of results of iterative reconstructions. This could be attributed to the fact that X-ray beam in 3rd generation synchrotron source is not fully coherent[16], the effect of partial coherence of X-ray probe might result to some imperfections to measurements, such as noises and reduced fringe visibilities, which eventually leading to partially unreliable data.

The following diagram shows general procedures of iterative algorithms for CDI reconstruction in Bragg geometry:

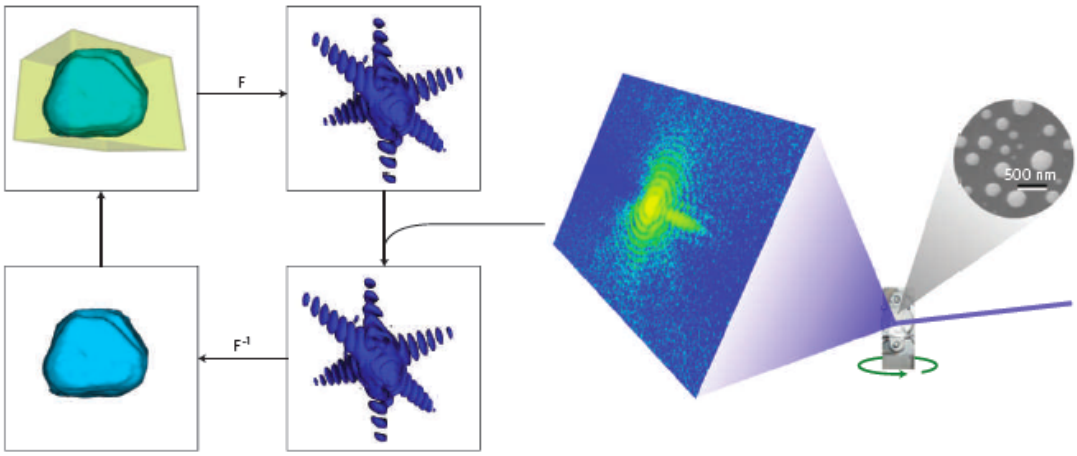

Fig. 5 The schematic diagram shows outline of the fundamental underlying algorithm that permits the reconstruction of a sample distribution from its diffraction pattern in Bragg geometry[19].

Initial guesses can be from either direct-space or reciprocal-space, whichever suits the best. In our case, initial random guesses from direct-space is implemented, with an initial guess of physical support in the direct-space with amplitude of random numbers inside the support, while amplitude is set to 0 everywhere outside the support. FFT is performed so that modulus constraint (keeping the phases values while replaces the amplitudes with square root of measured intensity of diffraction data) can be applied in reciprocal-space after 1st iteration of algorithms. The algorithm then does Inverse Fourier Transform to go back to direct-space to impose support constraint (where keeping the amplitude outside the support the same but making which are inside the support zero) by using Error-reduction (ER) step, where χ-square error metrics can be calculated. Alteration of ER with HIO algorithm shows better convergence and prevent stagnation of reconstructions, because the advantage of Hybrid-Input-Output (HIO algorithm over ER is that an extra feedback parameter β is introduced so that the algorithm is more likely to lift stagnation on the local minimum values of χ-square, in order to reach the true solutions of global minimum value of χ-square. Detailed analyses on error metrics of convergence success rates of different algorithms are illustrated in Garth William's PhD thesis[13].

2:2 Simulation studies on newly-invented revised Hybrid-Input-Output Algorithms

To start with random guess of electronic density and phase in direct-space of object

$$u_i^n = \left\{ \begin{array}{l} \tau_i,\ i \in Support \\ 0.0,\ \notin Support \end{array} \right\}$$

$$u_i^n = \left\{ \begin{array}{ll} \tau_i & i \in Support \cap \phi > \left(\phi_{\min} + \phi_{result\ of\ current\ iteration}\right) \cap \phi < \left(\phi_{\max} + \phi_{result\ of\ current\ iteration}\right) \\ u_i^{n-1} - \beta\tau_i & i \in Support \cap \phi < \left(\phi_{\min} + \phi_{result\ of\ current\ iteration}\right) \cap \phi > \left(\phi_{\max} + \phi_{result\ of\ current\ iteration}\right) \end{array} \right\}$$

$$u_i^n = \left\{ \begin{array}{l} \tau_i,\ i \in Support \\ 0.0,\ \notin Support \end{array} \right\}$$

New support: reset amplitude to random values but keep the phases of the last results as initial guesses of phases of support;

$$u_i^n = \left\{ \begin{array}{l} \tau_i,\ i \in Support \\ 0.0,\ \notin Support \end{array} \right\}$$

$$u_i^n = \left\{ \begin{array}{ll} \tau_i & i \in Support \cap \phi > \left(\phi_{\min} + \phi_{result\ of\ current\ iteration}\right) \cap \phi < \left(\phi_{\max} + \phi_{result\ of\ current\ iteration}\right) \\ u_i^{n-1} - \beta\tau_i & i \in Support \cap \phi < \left(\phi_{\min} + \phi_{result\ of\ current\ iteration}\right) \cap \phi > \left(\phi_{\max} + \phi_{result\ of\ current\ iteration}\right) \end{array} \right\}$$

$$u_i^n = \left\{ \begin{array}{l} \tau_i,\ i \in Support \\ 0.0,\ \notin Support \end{array} \right\}$$

Algorithms of revised Hybrid-Input-Output with Error-Reduction steps as complimentary analysis.

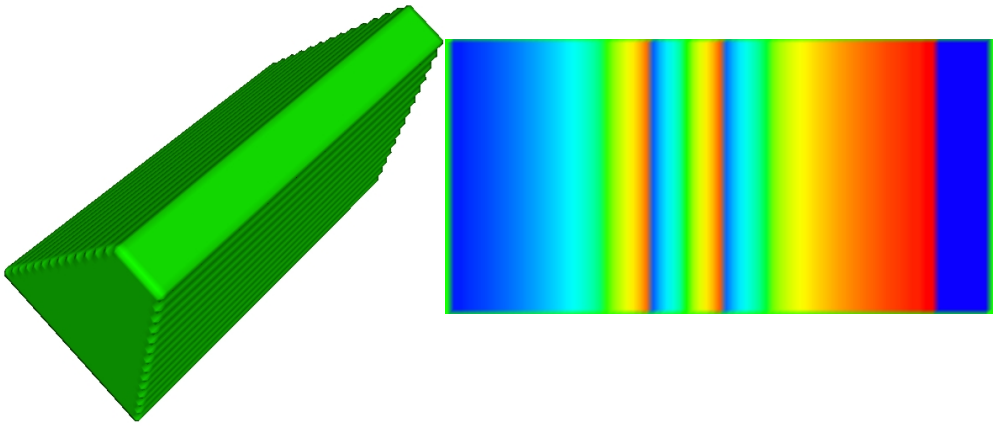

Fig. 6 Simulation of complex three-dimensional objects having the uniform density and right hand panel shows the phases, the blue and red colour representing $+\pi$ and $-\pi$ respectively, and the blue-red phase-wraps represent 2π of phase changes. The right hand side panel is the scalar-cut-plane of phase-values.

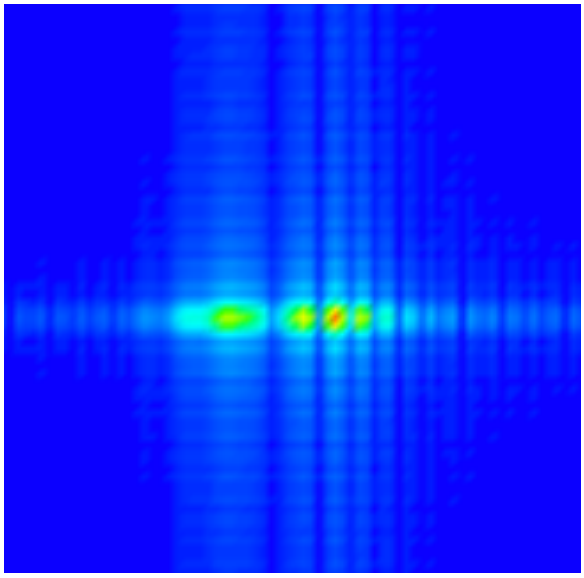

Fig. 7 Scalar-cut-plane of diffraction pattern of complex object in Fig. 6 of simulated amplitudes and phases, the cut is through the central slice.

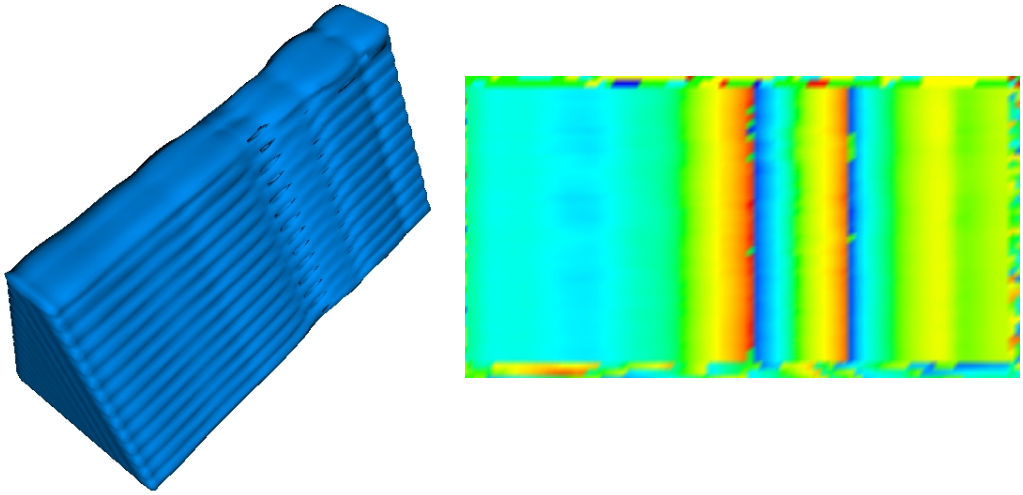

Fig. 8 Images show reconstruction of the diffraction patterns of simulated complex three-dimensional object above. Revised “phase shrink-wrap” algorithm is used in alternation with Error Reduction (ER) algorithm, i.e. the new combination of algorithms. There are no gaps and artefacts in the amplitude result and the phases are in a quite good agreement with initial simulation.

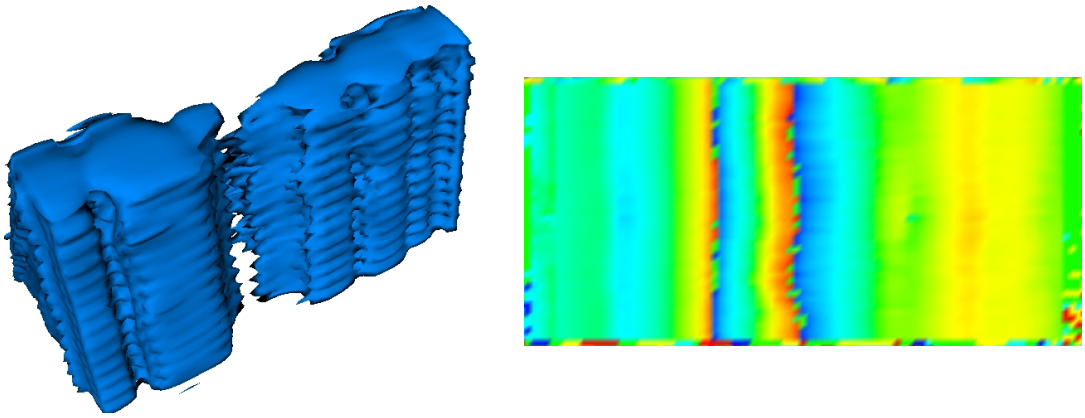

Fig. 9 Images show reconstruction of the diffraction patterns of simulated complex three-dimensional object above. Conventional phase-constraint Hybrid-Input-Output algorithm is used in alternation with Error Reduction (ER) algorithm. The reconstruction results clearly show gaps and errors as it might indicate failure of convergence of measurements, and the reconstructed phases show artefacts when comparing with the original designed phases in simulation.

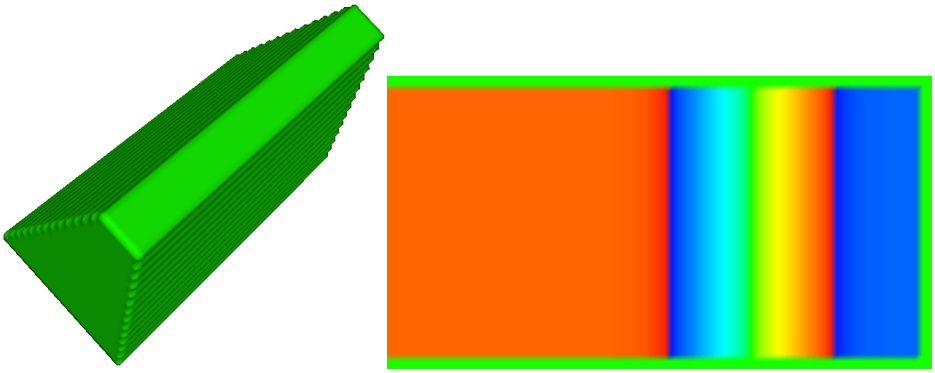

Fig. 10 Simulation of complex three-dimensional objects having the uniform density and right hand panel shows the phases, the blue and red colour representing $+\pi$ and $-\pi$ respectively, and the blue-red phase-wraps represent 2π of phase changes. The right hand side panel is the scalar-cut-plane of phase-values.

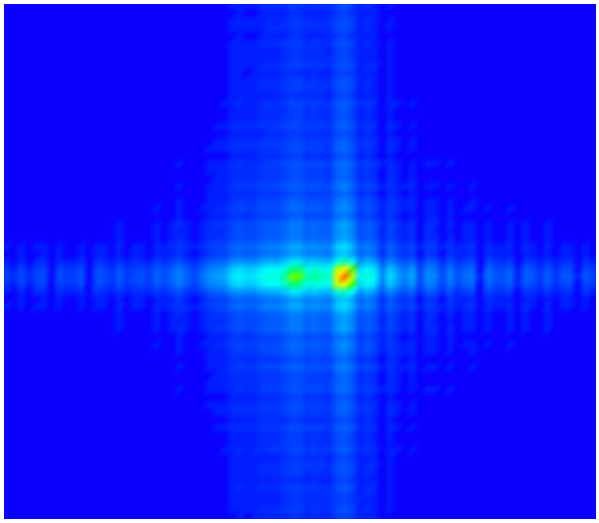

Fig. 11 Scalar-cut-plane of diffraction pattern of complex object in Fig. 10 of simulated amplitudes and phases, the cut is through its central slice.

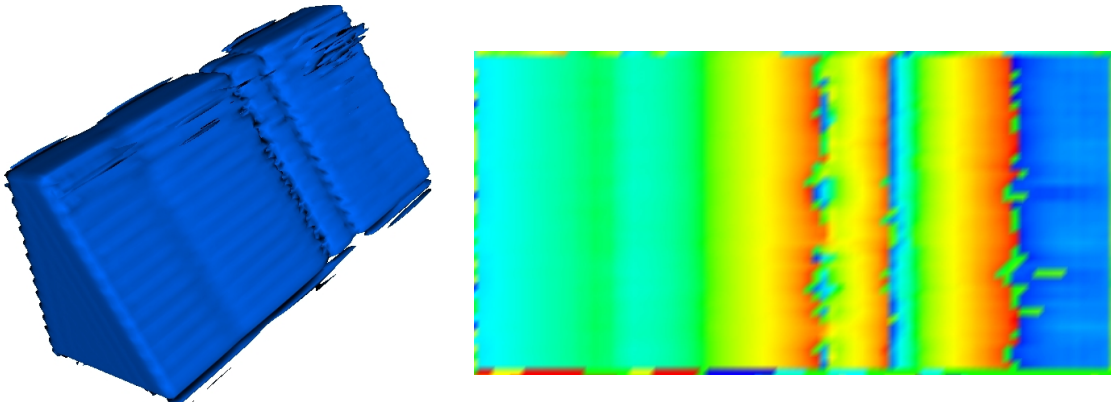

Fig. 12 Images show reconstruction of the diffraction patterns of simulated complex three-dimensional object above. Revised “phase shrink-wrap” algorithm is used in alternation with Error Reduction (ER) algorithm, i.e. the new combination of algorithms. There are no gaps and artefacts in the amplitude result and the phases are in a quite good agreement with initial simulation.

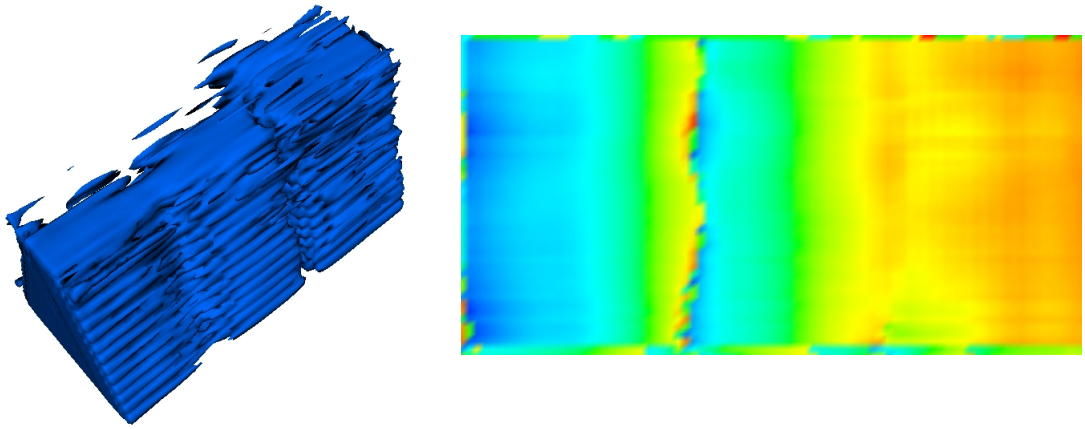

Fig. 13 Images show reconstruction of the diffraction patterns of simulated complex three-dimensional object above. Conventional Hybrid-Input-Output algorithm is used in alternation with Error Reduction (ER) algorithm. The reconstruction results clearly show gaps and errors as it might indicate failure of convergence of measurements, and the reconstructed phases show artefacts when comparing with the original designed phases in simulation. The reconstruction was performed with conventional ER + phase-

constraint HIO + ER algorithms, with 10 + 10000 + 10 iterations respectively. The result doesn't seem to converge correctly with noise reconstructed density. This is typical example that conventional CDI algorithms fail to work in highly strained cases.

Previous methods reported in literature for reconstruction with algorithms of different approaches of highly strained diffraction patterns on nano-crystalline structures have opened up a new path for better understanding of objects of highly complex wave functions[10, 26, 27]. Our newly revised HIO algorithm has been tested in simulated datasets, and highly strained simulated data with direct-space phase of up to 8π (which corresponds to 4 phase-wraps) was successfully reconstructed, both amplitude and phase were in a roughly good agreement with initial simulation, which shows significant improvements comparing with results with conventional HIO and phase-constraint HIO algorithms. The revised algorithm starts with initial random guesses of amplitude (standard polygon) and phase, follows by standard Error-Reduction algorithm and phase-shrink-wrap (revised) HIO algorithm with phase maximum and minimum of ½π and -½π respectively. A new complex support is created with amplitudes having values of initial random guesses (standard polygon) and with current values of phases from previous iteration copied to the support. Therefore, the current values of phases are used as guided initial values for the next iteration of revised HIO step. The new HIO algorithm takes the results of the previous phases as initial guesses to be constrained within ±½π for phase values within direct-space object to be reconstructed, alternating with standard ER algorithms to reach final convergence. The revised algorithm performs relatively better than conventional HIO algorithm because it fills the amplitude gaps of the reconstructed direct-space object by allowing phase-ranges to be extended around these regions; with the revised algorithm reconstructions usually converges after 3 steps of revised HIO with around 100 iterations for each step, though sometimes it takes a little bit longer to converge.

3 Important Theories of CDI and Bragg-geometry Ptychography

3:1 Propagation Uniqueness, Non-Gaussian Probe Illumination and Introduction of

Ptychography

Uniqueness problem in Coherent Diffractive Imaging (CDI) has been addressed by Rodenburg[28] and Huang[26], Huang has further confirmed such proposal on non-unique solutions of far-field CDI data reconstructions with simulations[26]. It has been proven in mathematical principles that if recorded diffraction data satisfy oversampling conditions[19, 29]. Nyquist sampling frequency is defined as the frequency of sampling to be twice the maximum frequency in reciprocal-space sampling frequency, which is the sampling frequency of the sample reciprocal-space lattice point. Furthermore, Nyquist sampling criterion states that in order to retrieve both electronic density (amplitude) and phase information from experimental diffraction patterns, the measured diffraction pattern sampling frequency has to be higher than the Nyquist sampling frequency. Sayre went on to propose his criteria of necessary condition for successful reconstructions of both electronic density and phase from measured reciprocal-space diffraction patterns of structures, one has to be acquire at least double amount of the sampling points of the reciprocal-space lattice frequency of measured structures[30], this proposal originates from the fact that both amplitude and phase information needs to be extracted, thus there are double amount of unknowns to be resolved comparing to the number of reciprocal-space sampling points in samples. Furthermore, It can be generally considered that to enable unique reconstructed solutions good quality of experimental measurements have to be obtained, which means the signal-to-noise-ratio (SNR) needs to be sufficiently high to gain useful data for reconstructions. Miao et al has performed detailed calculations to demonstrate that for two or three-dimensional datasets, unique solutions can be found if each dimensions having oversampling ratio of minimum value of $\sqrt[3]{2}$ or $\sqrt{2}$ for three or two-dimensional measurements respectively if overall datasets having oversampling ratios of at least 2, which in theory is sufficient for experimental data with satisfactory quality to be uniquely reconstructed[31].

$$t'(r') = \int t(r) e^{-ik(r-r')^2/2d} dr$$

Where d is the propagation distance of electromagnetic waves exiting from measured samples, i.e. the distances between different diffraction planes in the far field geometry.

Both $t(r)$ and $t'(r')$ are complex wave-functions of electromagnetic propagation which are exiting samples at positions d apart from each other. The complex electromagnetic wave actually propagate at infinite number of planes when exiting samples, however in this case, measurements are only taken at two planes separating with distance of d. Both $t(r)$ and $t'(r')$ yield the same solutions for direct-space reconstructions because they have identical patterns in Fourier domain. The solutions obtained depending on whichever constraints applied in direct-space part of algorithms, and different results are generated with different constraints, therefore, one has to have some priori-knowledge of samples if that is obtainable to select specific constraints in iterative reconstructions.

Both Huang[26] and Newton[27] have proposed modified algorithms for better reconstructions of highly strained Bragg-geometry CDI measured data with improved three-dimensional electronic density. The problem arises from the fact that with highly strained object, which is a specific feature when there is a significant strain in the sample that would cause phase shifts exceeding 2π (which is defined as phase-"wrap") between different parts of sample, might lead to reconstructions with amplitude having gaps in the phase-"wrap" regions. Newly invented constrains seem to make inversions better with results with most gaps filled in phase-"wrap" positions according to simulation studies in the previous part of the report.

Possible solutions to the above non-uniqueness problem are proposed, with the ones have most success are curved wave-front illumination which was demonstrated to have better convergence successes[9] in reconstructions such as wave front illumination with zone-plates. The key to solve the ambiguity problem is to break symmetry of entrance and exit wave functions and to reduce ambiguities of objects such as twinning, to be more likely to achieve unique solutions in CDI as a general.

Ptychography, both in forward transmission and far-field Bragg geometries, have demonstrated to be able to solve compact or extended structures with complexity[32, 33]. Recent work on studies of magnetic domain structures under evolution of magnetic hysteresis loops by using forward transmission geometry ptychography was reported[34]. It is believed that to be able to solve complex direct-space structures, overlap constrains in ptychography is a much stronger constraint when comparing with support constraint in CDI, both in forward and Bragg geometries. Nevertheless, uniqueness problem is still not completely

resolved by using better constraint alone, there have been some concerns on accurate reconstructions of phase structures of objects once probe structures are unknown, because the phase structures of probe and samples can be cancelled out from each other if they both have linear components. To improve the feasibility of successful recovery of both amplitude and phases of measured objects, systematic setups for measurements of probe structures have been developed at c-SAXs beamline at the Swiss Light Source (SLS). Ptychography with concentric-circle-scan[35] method have been developed and proven to improve data convergence and to reduce ambiguities in data reconstructions. It is advantageous over conventional rectangular-grid-scan due to its ability to break down translation symmetry, while the analytical descriptions of the scan positions can be preserved. This method has been proven to work relatively well in transmission geometry and it has been some success for implementation of the technique in Bragg geometry for Zeolite and SOI crystalline structures at beamline 34-ID-C at the Advanced Photon Source.

3:2 Bragg-Geometry Ptychography: Principles and Experimental Results

Demonstrations of Bragg-geometry Ptychography have shown the applicability of such technique with high degree of spatial resolution and reliability[36, 37]. To apply similar principles to Ptychography in transmission geometry, the Bragg case has better applications in compact or extended highly crystalline structures with its special emphasis on surface sciences, and three-dimensional atomic displacements fields can be reconstructed for a even single compact structure with current state-of-art instrumentations at available Bragg CDI beamlines worldwide, such as 34-ID-C at Advanced Photon Source and ID-1 at the European Synchrotron Radiation Facilities (ESRF). Bragg-geometry Ptychography has relative advantage over conventional Bragg CDI because of its much stronger direct-space overlap constraints implemented in the iterative algorithms for reconstructions. Such powerful direct-space constraint could in principle improve experimental data quality by providing users abundant two or three-dimensional datasets (for two or three-dimensional measurements respectively) from which users can easily discard any inappropriate sections of particular datasets due to its high degree of overlapping leading high degree of data

redundancy of the technique, usually between 50 to 80 percent. In contrast, conventional Bragg CDI has to reply on every single two-dimensional data sections to be of good quality in order to reliable data analysis. Furthermore, Bragg-geometry Ptychography is believed to have much more success for solving highly strained direct-space structures due to the nature of its data acquisition and algorithms, while such problems remain a difficulty in conventional Bragg CDI tough many attempts have shown improvements. Nevertheless, developments of algorithms and better quality of data acquisitions are needed for the next stage of this method, which is expected to have substantial impact on surface structures studies. Measurements of Round-Roi-Scan method have been performed at 34-ID-C at Advanced Photon Source for Zeolite crystals and SOI micro-squares. Our initial measurements show some encouraging results; however further studies could be vital aiming at better understanding of Ptychography of Bragg-geometry nature.

3:3 Optical Path-Length-Difference Induced Wave-Front-Difference of Coherent X-ray in CDI

To fully utilize the properties of Coherent X-ray at Coherent beamlines in 3rd generation synchrotron facilities, one has to make sure that both longitudinal and transverse coherence lengths have to be larger than the optical path-length-difference of coherent X-ray illuminating samples under investigations. Leake and colleagues have demonstrated[14] not long ago that varying optical path-length-difference of coherent X-ray illumination, which involves both reflection and transmission in Bragg geometry, can do measurement of visibilities of reciprocal-space diffraction fringes. These were performed by measuring different Bragg peaks of crystalline structures and also by recording varying coherent properties of incoming X-ray probe. Bean and colleagues have done detailed experimental work[38] on studying the relationship between fringe visibilities of reciprocal-space diffraction patterns and the overall optical-path-length-difference (OPLD) of incoming X-ray probe within samples, i.e. the OPLD of X- ray illumination. Nevertheless, the

measurements do not quite agree with theoretical hypothesis in which the group proposes that there is a direct relationship between the OPLD and the fringe visibilities such that the fringe visibilities decrease with increasing OPLD. The underlying basis for this hypothesis is rather subtle, since the bigger OPLD of incoming X-ray the higher probabilities of it exceeding either longitudinal or transverse coherence length, whichever is smaller in a particular situation depending on experimental conditions of X-ray probe and samples under study. Therefore, this hypothesis remains to be proven with possibly better experimental setups and other conditions, which are needed to be developed further.

4 Experimental results and theoretical work performed so far

4:1 Introduction of Silicon-On-Insulator (SOI) Technology

4:1:1 Silicon-On-Insulator

Silicon-On-Insulator (SOI) technology has been widely recognized as a major industrial breakthrough during the past decade, offering significant improvements of metal–oxide–semiconductor field-effect transistor (MOSFET) device performance [ref]. This is measured in terms of lower power dissipation, higher switching frequency and lower parasitic capacitance. SOI based MOSFETs are considered to be one of the best alternatives to conventional bulk-Silicon MOSFET technology, however, fabrication of SOI wafers are significantly more technologically challenging as the dimensions of the devices shrink dramatically [ref]. State-of-Art lithography-based fabrication techniques[39] are starting to be employed to overcome the possibility of strain arising from SOI fabrication[40].

4.1.2 SOI Fabrication Technologies

Various methods are used to fabricate Silicon-On-Insulator wafers: hetro-epitaxy, Separation by Implantation of Oxygen (SIMOX) [41, 42]and wafer bonding followed by Smart Cut^{TM} technology[43, 44]. The SIMOX technique is particularly widely used due to relatively low crystal-defect density, low variation of film thickness and high crystalline-quality leading to high-quality wafers with high charge-carrier mobility. The SIMOX process involves Oxygen ion implantation onto single-crystalline Silicon wafers, during which oxidation occurs; a

subsequent high-temperature annealing process recovers the high-quality crystalline structure of film. Smart Cut^{TM} technology involves transferring high-quality single crystalline Silicon thin layer from wafer to wafer after bonding, and is followed by annealing and final polishing processes.

With SOI technology, there is concern that crystalline defects and lattice imperfections might cause various problems for high performance devices, by shortening the device lifetime or reducing the efficiency of performance. This invites the use of high-resolution X-ray diffraction methods. In previous work, SOI bare wafer structure; highly-strained SOI and Strained-Silicon-On-Insulator (SSOI) nanostructures have been studied and characterised by coherent X-ray diffractive imaging technique[5, 26, 27, 45]. SIMOX material is unsuitable for the experiments because the device and substrate "handle" layers would be exactly aligned, so signal from the thin film would always be swamped by that of the substrate.

4:2 Measurements and results on SOI un-patterned wafer

This work has been published in 2010 with the following reference:

Structural inhomogeneity in Silicon-On-Insulator probed with Coherent X-ray Diffraction Xiaowen Shi, Gang Xiong, Xiaojing Huang, Ross Harder and Ian Robinson, *Zeitschrift fuer Kristalographie* 225 610-615 (2010)

All authors of this paper have contributed to the work illustrated below.

4.2:1 Micro-beam Diffraction of SOI wafers

All the measurements reported here were performed at beamline 34-ID-C of the Advanced Photon Source at Argonne National Laboratory. These measurements were performed by scanning a focussed 8.902keV X-ray beam across the sample while recording the diffraction pattern of an off-specular 111 reflection on a direct-detection CCD detector positioned 1.8m away from the sample. A grazing incidence angle of 5º was employed. The beam was focussed by Kirkpatrick-Baez (KB) mirrors to a probe size of about 1.5 microns and was made coherent by entrance slits of 10x20 microns placed before the mirrors. The beam was scanned along the direction parallel to the SOI surface and perpendicular to the beam

direction (called “X” here) to study the variation of topography and mosaic structure of a typical SOI wafer.

Figure 14 shows key features extracted from the micro-diffraction measurements, after removal of positions, which showed little variation. In many positions along the scan, there was just a single peak recorded, which varied in position on the detector, while in the positions highlighted there were two or even three peaks seen. The (x,y) position on the detector was converted into (roll,pitch) angular motions of the crystal lattice planes. The same scan performed on a standard Si(111) wafer showed no variation of peak positions, so the observed effect is not a property of the mechanical scanning stage (Newport model MFA) or other instrumentation. The typical distance in X-position from one-peak to two-peak of diffraction patterns or two-peak to three-peak is around 10 steps (5μm), which indicates that an average feature size is about 5μm. A similar scan along the Y-direction showed very little variation of diffraction patterns, presumably because the X-ray beam footprint along that direction is much longer, about 15 μm.

The results show strong variations of the centre of the rocking curves with splitting and de-splitting of peaks along this particular scanning path. The variations of positions of the peak maximum were due to surface topography or structure inhomogeneity of the SOI wafer, which might be a direct consequence of the film-transfer steps of the wafer fabrication procedure. Since it is possible the defects could affect the electrical properties of the material, it would be useful to apply this method as a routine diagnostic of the film transfer procedure.

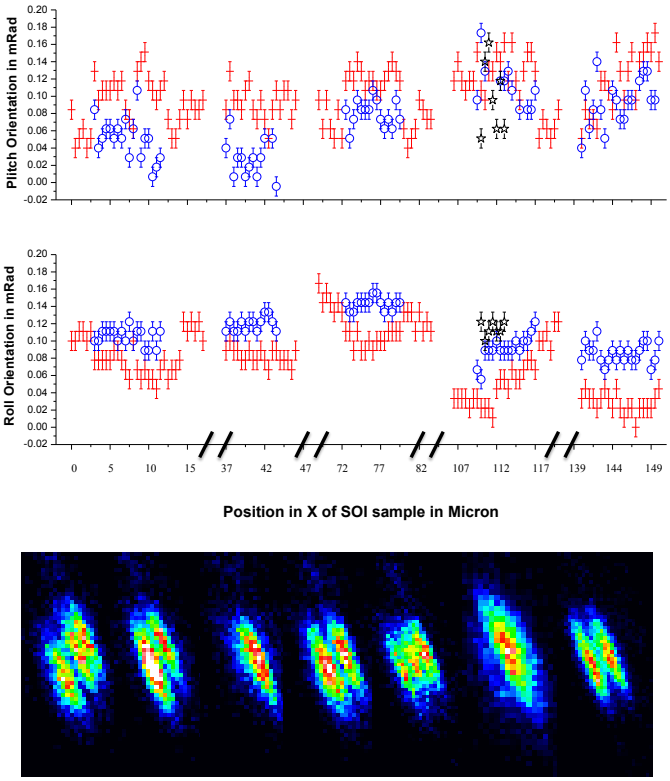

Fig. 14 Micro-beam diffraction of a typical SOI wafer. Upper panels: Roll(X direction) and Pitch(Y direction) orientations vs. position along X direction. The red, blue and black symbols represent the various positions of the peak maxima on the CCD. Some points where only a single peak was present have been removed. The pitch direction deviation is slightly bigger than that of the roll direction. The scan was performed with 5º of incidence angle, and 1800mm distance between the CCD detector and the specimen on the off-specular (111) reflection. Bottom panel: appearance on the CCD of micro-beam diffraction patterns at various X positions separated by around 9 microns. The intensity scales are the same for all patterns in the bottom panel. Figure is from [45]

4.2.2 Mosaic Structure and Split Diffraction Peaks

Splitting of peaks into two or three occurs when two distinct orientation are present in the sample at the same time. In a simple incoherent-beam model, the presence of two distinct peaks, rather than a smeared distribution, would mean that there is a sharp boundary between the grains, as in the classical picture of mosaicity. If clean fractures were present, passing right through the film, as suggested, this might have consequences for the electrical properties of the material. Mosaic structure in thin film single crystalline Silicon would be accompanied by dislocations or lattice faults between the crystal grains. In this model the peaks arise from the specific positions of the mosaic blocks within the whole structure; in this case it is the summation of the diffracted intensities which can be very different for adjacent locations due to the variation the orientations of mosaic blocks. This would be expected to give abrupt jumps in otherwise straight lines tracking the peak positions, as illustrated by the solid lines in Figure 15.

In our experiment at APS, the beamline was designed to preserve the coherence of the X-rays. A coherent X-ray entering more than one mosaic block would result in interference patterns, resulting from linear superposition of the diffracted waves. This leads to an alternative explanation of the splitting of peaks because the contributions of neighbouring grains add coherently. Even if there are continuous variations of orientation between strained regions of single-crystalline structure, distinct peaks will arise because of the coherence. In a general way, the splitting of peaks can be modelled by a spatial variation of real-space phase, which can be linear ramps, parabolic or more complex phase variations. An active field of research is looking into the kinds of phase structure that can explain complex mosaic structures by coherent X-ray diffraction.

The dashed lines in Fig 15 show schematically what we expect would happen under coherent X-ray illumination conditions. As interference effects turn on there would be a gradual shifting of the peaks, along with intensity variations. Even abrupt boundaries between undistorted mosaic blocks (as illustrated) would lead to smooth variations in peak position. In Fig 15 we see smooth evolution of the peak positions, but this does not allow us to tell whether the boundaries between mosaic regions of our SOI sample are abrupt or continuous. Further quantitative work should be able to answer this technologically important question.

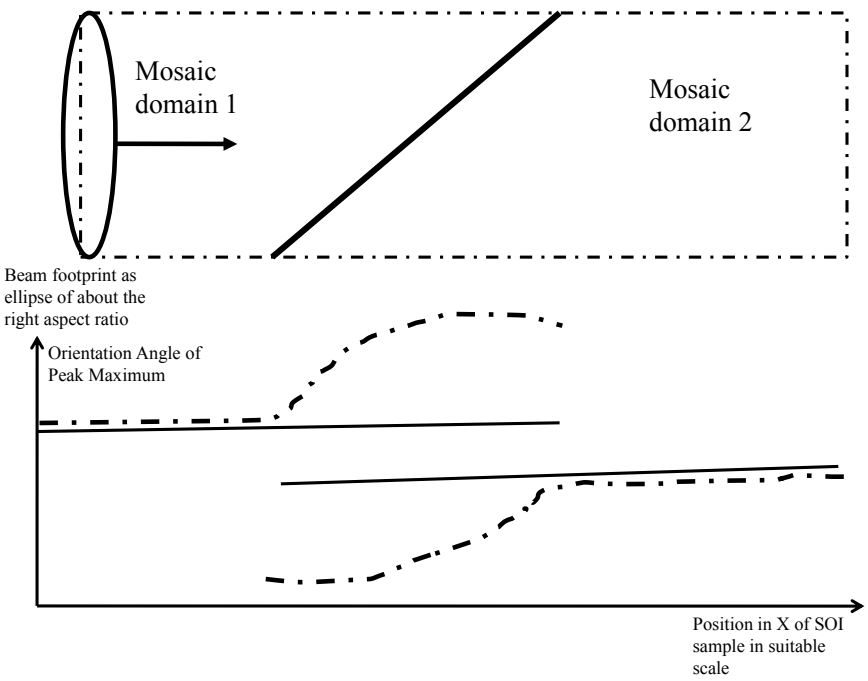

Fig. 15 Illustration of the coherent and incoherent limits of diffraction from two overlapping mosaic grains. Upper panel: The black dotted line represents the edge of the object under study. The diagonal line represents a grain boundary separating two crystal mosaic blocks adjacent to each other. Lower panel: lines representing the positions of the peak maximum of diffraction patterns as a function of location of such a multi-grain crystal. The solid and dashed lines represent the expected variation in the fully incoherent and coherent limits respectively. Figure is from [45]

4:3 Measurements and simulation analysis on highly–strained SOI nanowires

This work has been submitted to New Journal of Physics (IOP) on 23rd of March, 2012 with the following reference:

Radiation induced bending of Silicon-On-Insulator nanowire probed by coherent X-ray diffractive imaging Xiaowen Shi, Gang Xiong, Xiaojing Huang, Ross Harder and Ian Robinson, submitted to *New Journal of Physics* (2012)

All authors of this paper have contributed to the work illustrated below.

4:3:1 Strained SOI nanowires Sample preparation and fabrication procedures

We have performed characterisation of highly strained SOI nanowires by coherent X-ray diffractive imaging method, which quantitatively reveal direct-space images of displacements due to defects or dislocations etc. within structures of measurements with a resolution potentially reaching tens of nano-metres. In our experiments, we used wafer bonded samples instead to avoid the difficulties with SIMOX mentioned above. A Silicon (111) substrate ("handle") was employed to have a different crystallographic orientation from that of the top Silicon layer (001) studied. This allowed the diffraction signal from the active top Silicon layer to be independent of interference from the substrate.

The strained Si layers on insulator wafers used in this study were fabricated by using wafer bonding and a thin layer transfer method. It consists of a 170nm thick Si thin film on top of a silicon oxide capped Si substrate, and the oxide layer is 1μm thick. Both of the Si layers are grown along the (100) direction, but their in-plane orientation is shifted 45 degree away from each other during the bonding process. This is to eliminate the signal from the substrate during the CDI measurements. Extended ordered arrays of Si nano wire structures with a lateral dimension in the range of 400-1500 nm, length of 15 μm, separated by 100 um both horizontally and vertically, were patterned on a PMMA resist using electron-beam lithography. Reactive ion etching (RIE) was then applied, using SF_6 at a flow rate of 30 sccm and DC voltage of 100V, to transfer the pattern to the top Si layer, leading to ordered arrays of Si nano wire structures directly on SiO_2.

Reactive ion etching results in either straight or undercut sections of Silicon nanostructures for our measurements. Chlorine-based etching technique will be used for comparison with SF_6 etching technique in the near future.

The Silicon wires and dots of interest were fabricated with various shapes and sizes. The Silicon wire used for the measurements in our study had dimensions of 15µm x 800nm x 170 nm (length x width x height), starting from a 170nm SOI wafer.

4:3:2 Coherent X-ray Diffractive Imaging measurements on highly strained SOI nanowires

The samples were aligned on the off-specular (111) reflections with an incidence angle of 1 degree, and the CCD detector with 20 µm pixels was placed 1.2 meters away from the sample at the correct Bragg angle, theta. Three-dimensional rocking curves were measured at a particular Bragg reflection of Silicon by rocking specimen around ±0.5 degree in theta steps of 0.005 degree so that oversampling conditions in all three reciprocal-space spatial dimensions satisfied.

4:3:3 Results of Experimental Measurements

Fig. 16 shows a series of measured diffraction patterns with increasing X-ray illumination dose on a typical SOI nanowire (with spatial dimensions of 1.5µm X 800nm X 170nm). The peak shape is three dimensional in the space of ($X_{detector}$, $Y_{detector}$, θ), so the views shown are two-dimensional scalar-cut-planes in the direction of greatest elongation. Fig. 16 shows a typical diffraction pattern from a nanowire crystal with very little internal strain. It can be clearly seen that the central peak of the pattern is just about to split into two peaks; this might indicate that internal strains are just being developed during measurements, with evolution of peak splitting in the early stage where multi-peak patterns are starting to appear, and finally show gradual increase of peak-splitting in the data for longer X-ray exposure. One can deduce that the underlying mechanism of this peak-splitting effect must be due to the X-ray dose, due to the fact the measurements were performed at exactly the same position on the

chosen nanowire with the same experimental parameters for data acquisition. The peak-splitting effect originates from of the accumulated X-ray exposure or received dose.

The reciprocal-space unit lattice-vectors for all directions of experimental measurements are evaluated by the following expressions:

$$\Delta q_{\chi,y} = \frac{\Delta p_{\Delta x,\Delta y} \times P}{D} \times \frac{2\pi}{\lambda} \ (nm^{-1})$$

$$\Delta q_{\theta} = q \times \Delta\theta = \frac{2\pi}{d_{(111)}} \times \Delta\theta \ (nm^{-1})$$

(eqn. 1)

Where $\Delta p_{\Delta x,\Delta y}$ are the reciprocal-space unit vector in $X_{detector}$ and $Y_{detector}$ dimensions, P is widths of peak envelope distribution in pixels on the detector, Δq_{θ} is the reciprocal-space unit vector in θ (rocking) direction, $d_{(111)}$ is the lattice-spacing of Silicon (111) direction, D is sample to detector distance and λ is the wavelength of incoming X-ray.

The peak splitting effect is in both the XY plane of the detector and an offset in the Bragg angle theta. The combined splitting in units of Δq is plotted against exposure time in Fig 17. It can be recognised that the measured three-dimensional splitting increases approximately linearly with time of exposure of the X-ray beam on the single location on the chosen nanowire. The plots of widths of split-peak as a function of X-ray illumination dose for three separate datasets from three different SOI nanowires are shown in Fig. 17. A similar trend is seen in all cases.

A block of Si illuminated by the focussed X-ray beam should give the diffraction pattern of a slit, i.e. a sinc function, in the two directions perpendicular to the wire; along the length of the wire the pattern is expected to be roughly Gaussian corresponding to the Fourier transform of the beam profile. In this model there would be a single central peak and no splitting. The peak splitting of the 3D diffraction data can only be related to the introduction of a significant strain in the sample that would cause phase shifts exceeding 2π (which is defined as

phase-"wrap") between different parts of the illuminated part of the sample[19].

One model is to introduce strain as a quadratic variation of phase along the sample[46]. This gives rise to a diffraction pattern that resembles a Fresnel integral[46]. Roughly speaking, the number of peaks in the resulting diffraction pattern corresponds to the number of "phase-wraps", i.e. the number of 2π repetitions within the illumination region of the nanowire. The linear splitting of the peak with dose would correspond to a linear increase in the quadratic phase or a linear increase of strain. Specific physical or chemical properties of SOI nanowires could contribute to various patterns of strain leading to this linear dependency. These will be investigated in this paper by appropriate modelling.

The 34-ID-C beamline at Argonne has an integral confocal optical microscope used for 3D alignment of the sample in the beam[47]. This microscope was used to capture the confocal image in Fig. 18 immediately after the dosing series. Fig 18 shows a height difference between a dark band and the rest of the surface. The dark band has the shape and size of the X-ray beam footprint due to the angle of incidence of 1 degree. The focal depth of the confocal microscope was measured to be 100nm approximately, and the image contrast indicates that the height difference of radiation-damaged regions of Silicon and oxide and the non-or little damaged ones is of the order of around 10nm. One can see that the burn is clearly extending over the oxide region, rather than the nanowire itself, which appears intact. So we can hypothesize the distortion comes from radiation damage to the Silicon Dioxide.

Therefore, we propose a model in which SOI nanowires of large internal strains in our measurements is likely to be the consequence of a radiation-induced bending effect. This originates from a time-dependent thickening of the Silicon dioxide layer below the patterned Silicon nanostructures during the X-ray irradiation. The rate of thickening of the bottom part of Silicon nanowire layer is proportional to the time of exposure of X-ray, in other words, the accumulated dose. To confirm our radiation induced bending effect model, measurements of three-dimensional rocking curves of different nanowires were performed in a Helium gas-filled chamber. Much less radiation-bending effects were observed with little peak-splitting after 2-hour of exposure, corresponding to the same dose per unit area on the sample.

This observed important peak-splitting behaviour might be related to a specific SOI wafer

bonding technique, which can be different from other methods. There have been no observed radiation-induced bending effects in some other measurements of SOI structures[5, 26, 48]. Radiation effects in SOI have been reported by the authors of ref [49], who observed structural change due to radiation damage on SOI nano-structures with an oxide layer underneath. However, radiation damage was not observed with SiGe thin-film structures on Silicon substrate only with no oxide layer in between, therefore the report suggests that the causes of radiation damage on Silicon or SiGe structures originated from the oxide layer or the interface between the Silicon and oxide layers [49]. This conclusion is consistent with what we have observed in our measurements.

4:3:4 Finite-Element-Analysis (FEA) calculations

FEA calculations were performed by using the COMSOL Multiphysics® package. A model structure was composed of a Silicon layer of 6μm (x) × 800nm (y) × 170nm (z) on top of a SiO_2 layer, all of which are sitting on bulk Silicon substrate. The SiO_2 layer is divided into two parts: one part designated for the application of isotropic stress with selected box-shaped region directly underneath the top Silicon layer of dimensions of 3μm (x) × 800nm (y) × 600nm (z), the other part with no initial stress applied in the simulation. Since we assume that the underlying mechanism of the peak-splitting effect is a consequence of pressure from the Silicon Dioxide that is closest to the patterned Silicon layer, we model a one-dimensional stress following the shape of the X-ray beam. A one-dimensional isotropic Gaussian stress was programmed within this box as a function of x only. The simulated Gaussian stress has 0.9 μm FWHM and it is centred in the middle of the wire so that it is symmetric function with a maximum stress of 300MPa (N/m^2).

Simulation results are shown in Fig. 19 with detailed displacement fields of x and z-components with axes marked on Fig. 19. One-dimensional line plot in x-direction of the simulated model (in central line of the top Silicon layer) is illustrated in Fig. 20. The output of the simulation is a displacement field within the model Si wire in physical units (m). This has to be converted into a real space phase in order to calculate the expected diffraction pattern. The conversion of $\vec{u}_{x,y,z}$ to a phase requires the experimental diffraction vector $\vec{Q}$, in this

case the (111) reflection of Silicon corresponding to the 3.1350Å silicon (111) lattice spacing. The real space phases due to atomic displacements of Silicon (111) reflection can be calculated by the following formula:

$$\text{phases}\,(\text{radians}) = \text{Si}(111).\vec{u}_{x,y,z} = \frac{\text{direct-space displacements (along } \vec{Q})}{\text{Silicon}\,(111)\text{ lattice-spacing}} \times 2\pi$$

(eqn. 2)

Where $\vec{Q}$ is the reciprocal-space lattice vector, and $\vec{u}_{x,y,z}$ are direct-space displacement fields in all three spatial directions, the dot product $\vec{Q}.\vec{u}_{x,y,z}$ gives evaluation of phases along direction of $\vec{Q}$.

For transformation to reciprocal space, the FEA object was sampled on a grid of 100, 30 and 12 pixels in x, y and z directions respectively. This object was zero padded into a larger array of 256, 128 and 128 pixels to avoid aliasing effects when the FFT was then calculated.

In order to simulate the diffraction patterns, the X-ray beam profile also has to be taken into account. The beam profile was assumed to be Gaussian amplitude (with zero phase) having a Full Width at Half Maximum (FWHM) of 16 pixels in x direction. The total number of pixels incorporated into our simulations in the x direction was 100. This width was chosen to be the same as the width of the stress profile used to generate the pattern of distortions in FEA. This profile was used as the amplitude of the object whose phase is given by Equ 2 above. Fig. 21 displays x-y view of scalar-cut-plane of simulated phases of our direct-space model for various maximum values of applied Gaussian stress function on the oxide layer.

4:3:5 Conversion to three-dimensional diffraction patterns

The diffraction pattern A(q) of an electron density distribution $\rho(x)$ is connected by the analytic continuous Fourier Transform (FT). This is expressed with the following formula:

$$A(q) = \int_{-\infty}^{\infty} \rho(x) e^{iqx}\, dx$$

(eqn. 3)

To convert this to numerical Discrete Fourier Transform (DFT), the continuous functions need to be written as arrays of complex numbers. Theoretical oversampling ratios of 2.56, 4.3 and 10.7 were introduced for x, y and z direct-space directions respectively. The sampled quantities are array of complex numbers: A_j and ρ_k, where the real and reciprocal space variables have become discrete $x = \Delta x.k$, $q = \Delta q.\, j$.

$$A_j = A(\Delta q.j)$$
$$\rho_k = \rho(\Delta x.k)$$

(eqn. 4)

The DFT connection between arrays is:

$$A_j = \sum_{k=0}^{N-1} \rho_k\, e^{2\pi ijk/N}$$

(eqn. 5)

The exponents in the expressions for the FT and DFT have to be the same, which means:

$$\frac{2\pi}{N} = \Delta q.\Delta x,$$

We note that the physical quantities Δq and Δx have units of m and m^{-1} respectively. N is the dimension of the arrays. Array sizes used in simulations are of N=256, 128 and 128 pixels in x, y and z dimensions respectively.

4:3:6 Discussion

The direct comparison of our measured and simulated diffraction patterns of radiation-induced bended SOI nanowire is shown in Fig. 22. Inspection of these and the data in Fig 16 reveal a very close resemblance in both two-dimensional scalar-cut-planes and one-dimensional line plots, confirming the appropriateness of our model. The model parameters have been adjusted to get some quantitative understanding of the radiation-induced bending effect on SOI nanowires

The beam size used in the simulation agrees well with wire-scan estimates. The model we constructed assumes a similar sized beam for the cause of the damage (stress profile shown in Fig. 21) as for the diffraction pattern. When one or other width was varied, the agreement of experiment and model was found to become worse. Our analysis shows that the best fit to the measured data in Fig. 22 has Gaussian stress function applied to the oxide layer and X-ray Gaussian probe with FWHM of 0.9 and 1.0 μm respectively.

The other parameter in the model that is very sensitive is the peak value of the applied Gaussian stress profile. This peak stress was varied systematically in Fig. 23, which shows widths of the simulated peaks (defined in the same way as for the experimental data in Fig 17, converted into reciprocal-space lattice units) as a function of maximum values of Gaussian function of stresses applied in the oxide layer. The behaviour is quite accurately linear, as expected from linear response theory, but confirmed through the FEA simulation. The widths of peaks are also roughly proportional to the number of 2π phase-"wraps" in direct-space phase structures of simulated object, as seen in Fig 21.

We can compare of the simulated diffraction response in Fig 23 with the experimental observation as a function of X-ray dose in Fig 17. Both curves are linear, although different samples have slightly different slopes. Equating the slopes of Figs 17 and 23 allows us to calibrate the rate of generation of stress by X-ray irradiation of SiO_2. The peak width reaches $0.04nm^{-1}$ after 100mins or 200mins depending on the sample. This corresponds to a peak stress of 185MPa according to the simulation in Fig 23. The coherent flux of the

beamline is not well-calibrated, but is roughly 10^9 photons/sec integrated over the focal spot with an area of $(1.5\mu m)^2$. A 100 min exposure would cause 6×10^{12} photons to be absorbed, depositing an energy of 0.009 J within a volume of 1.5μm×1.5μm×180μm (penetration depth of SiO_2 at 8.9keV), with a mass of 0.9×10^{-12}kg, amounting to a dose of 1×10^{10}Gy (J/kg). Dividing these quantities indicates a stress of 0.0185 Pa/Gy of dose for the first sample, 0.037 and 0.0925 Pa/Gy of dose for the second and third samples respectively.

4:3:7 Conclusion and Future Outlook

Our results show that damage introduced in the oxide adjacent to a lithographed Si nanostructure can result in significant strain in the device. It might be possible to use this or related methods of modifying the oxide to engineer strain for device applications. It has been found that strains induced in Silicon-based devices during fabrication processes can result in enhanced channel mobility[50]. Band gaps of strained nano-sized semiconductors can be modified[51] and strained Silicon band gaps have been theoretically predicted to switch from indirect to direct[52].

We have demonstrated the power of the Coherent X-ray Diffraction (CXD) analysis method based on Bragg peaks is highly sensitive to strains in crystals. We would hope this method and future Bragg-geometry ptychography techniques will encourage further studies on SOI based devices, which could be vital for pinpointing underlying mechanisms that are responsible for observed improvements on carriers mobility. For example, it has been shown that SiGe cylindrical core-shell nanowire based NWFETs demonstrate significant improvements on electron/hole charge carriers mobility and device efficiency[53]. Some recent work of successful studies of three-dimensional Bragg ptychography on Silicon-On-Insulator structures were reported[48]. This may open a new path for direct-observation and in situ characterisation of nanostructure semiconductor devices ranging from sensors and optoelectronic devices.

In the future, we plan to use the COMSOL-based simulations to improve the algorithms for CDI. The present CDI method uses a Hybrid-Input-Output Algorithm[54, 55] in alternation with conventional Error-Reduction algorithm[55] to phase the oversampled diffraction patterns measured by CXD. However this approach generally fails for reconstructing the diffraction patterns of highly strained objects. We plan to use simulated models as starting points for reconstruction of experimental data, solving for the deviations from an already close model. We believe that if the phase errors are less than π, the stagnation of the current algorithms will be avoided. Our initial results give us some optimistic results and detailed studies have been under development to be reported in the near future.

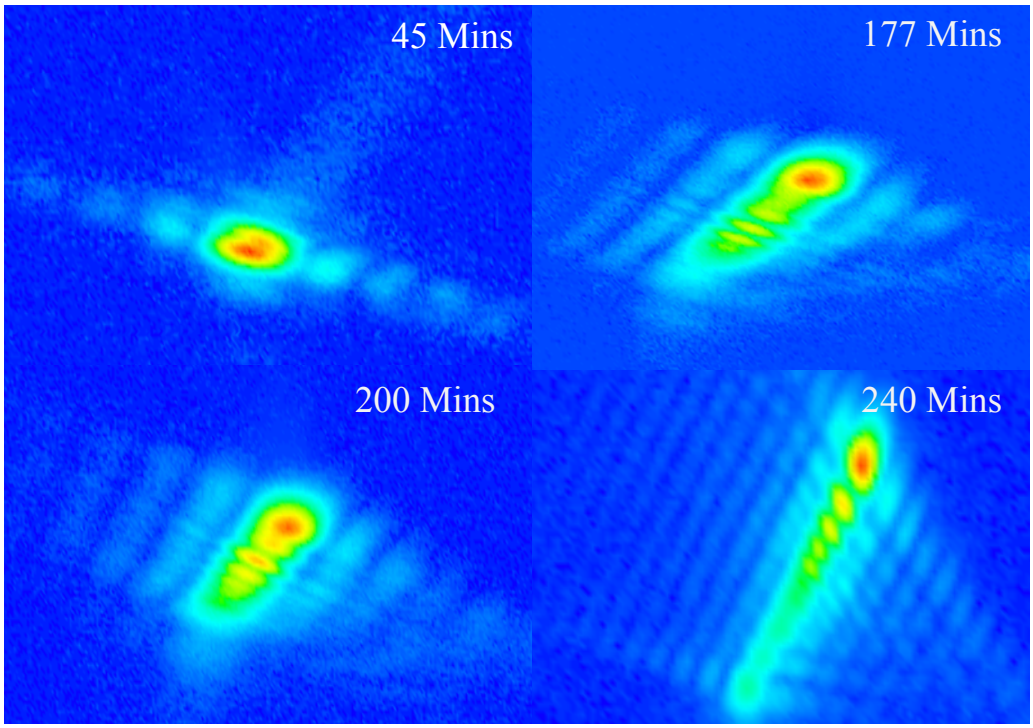

Fig. 16 Central slice of intensity of the measured three-dimensional diffraction patterns, showing the evolution of diffraction peak splitting with increasing X-ray doses. Each image shows the same two-dimensional scalar-cut-plane through the full three dimensional diffraction pattern. All of the images are measurements on the same region of a single SOI nanowire. The X-ray probe illumination dimensions of 1.5μm X 800nm X 170nm for length, width and thickness respectively.

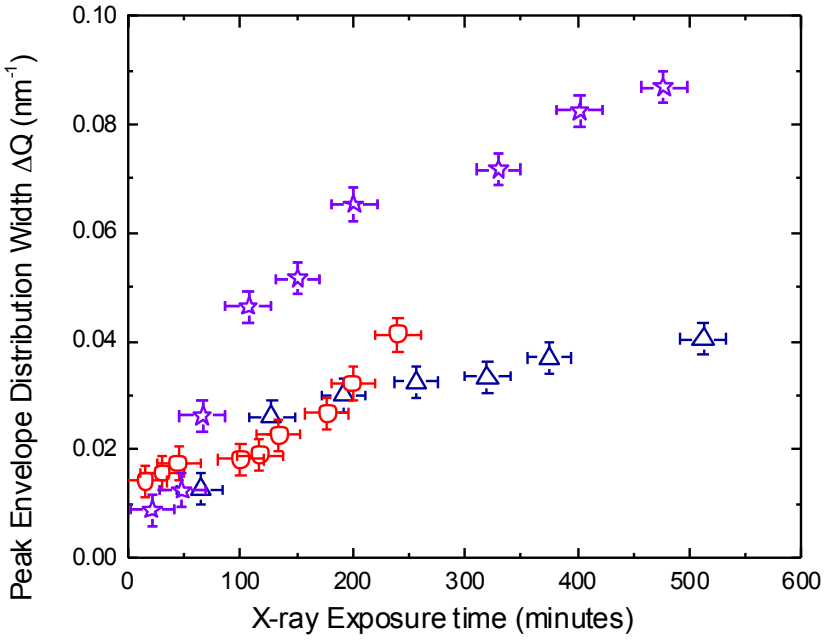

Fig. 17 Widths of split-peak distributions (in reciprocal lattice units) as a function of X-ray dose of the measured diffraction patterns. The behaviour is roughly linear for all three different datasets. The blue, red and purple datasets groups were measurements taken for different SOI nanowires with the same spatial dimensions of X-ray probe illumination.

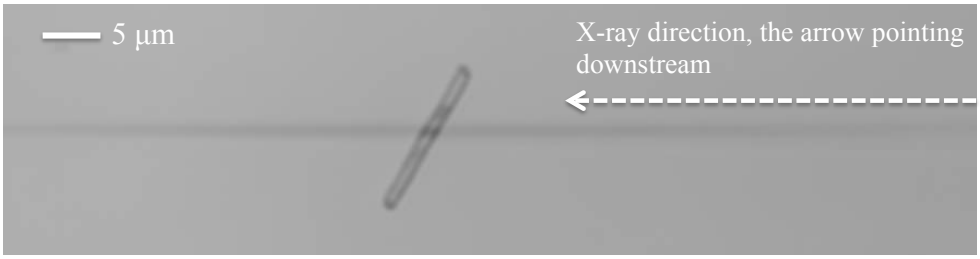

Fig. 18: Confocal microscope image of one of the SOI nanowires after dosing with X-rays for about 2 hours. The X-ray beam is inclined at a 1-degree incidence angle, running right to left. The surface of SOI nanowire also appears to have become raised by the beam exposure. The darker colour represents higher level of the SiO_2 surface under the beam illumination footprint. This image was captured with Olympus LEXT instrument with a laser wavelength of 408nm.

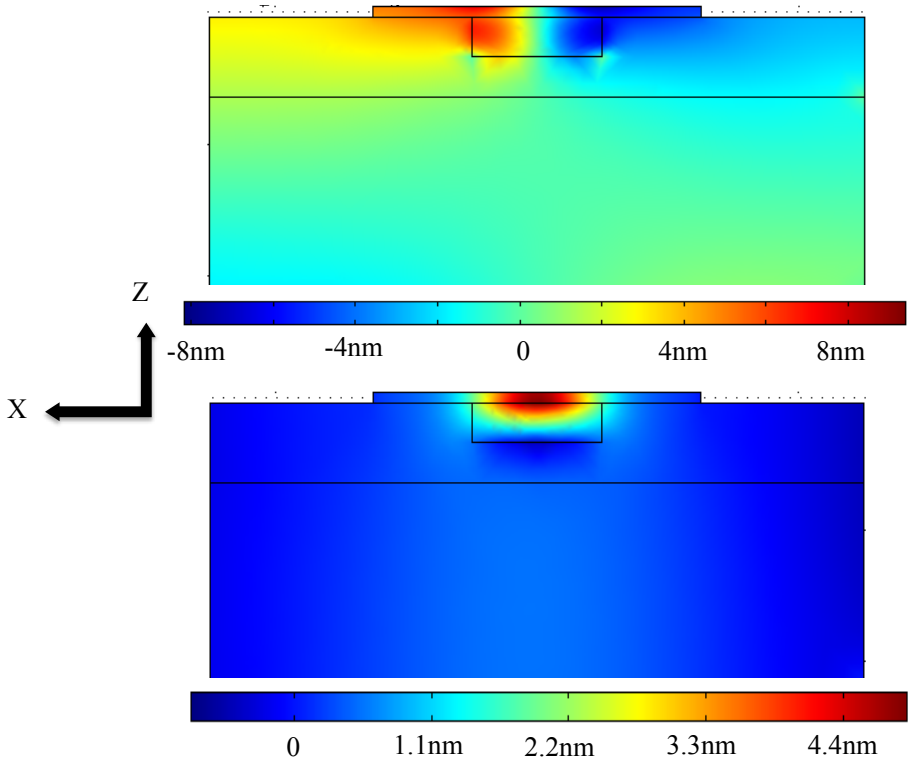

Fig. 19 Finite Element Analysis (FEA) calculation result showing *x* displacements (top) and z displacements (bottom) of a Silicon wire structure modelled on a SiO_2 substrate block and Silicon substrate. An isotropic Gaussian stress of 0.9µm FWHM length, centred in the middle of the SiO_2 block as a symmetric function, has been applied in the box-shaped region

below the wire. The maximum stress is $3x10^8$ Pa (N/m^2).

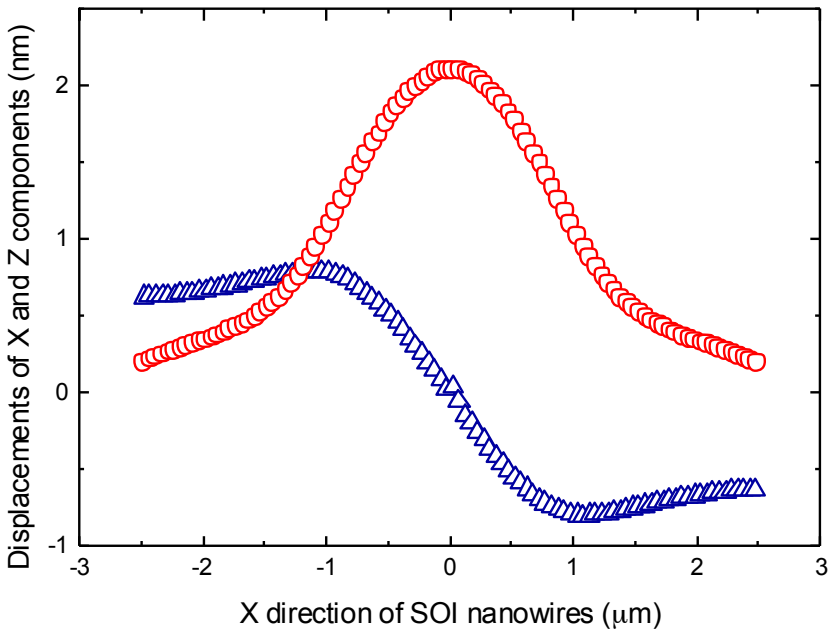

Fig. 20 Line plots of the x (blue triangles) and z (red circles) components of displacements from the FEA calculation in Fig 19, extracted from the surface of the central slice of the SOI model system.

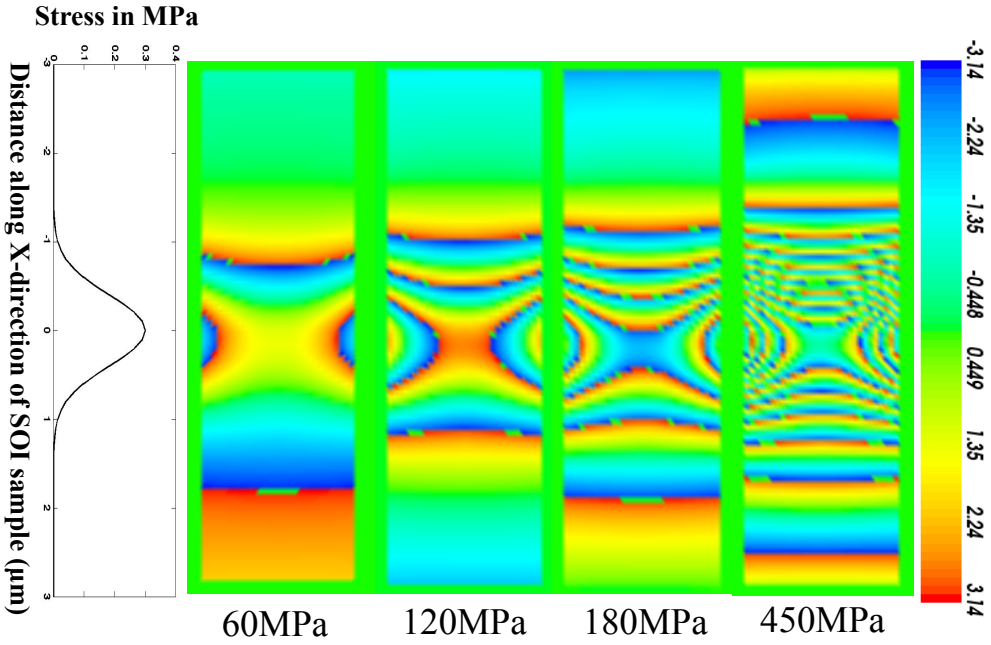

Fig. 21 Simulated direct-space phase images of the FEA -calculated displacement fields, as viewed from the top of the Si nanowire (x-y plane). The labels give maximum values of the one-dimensional Gaussian applied stress functions, shown schematically on the left.

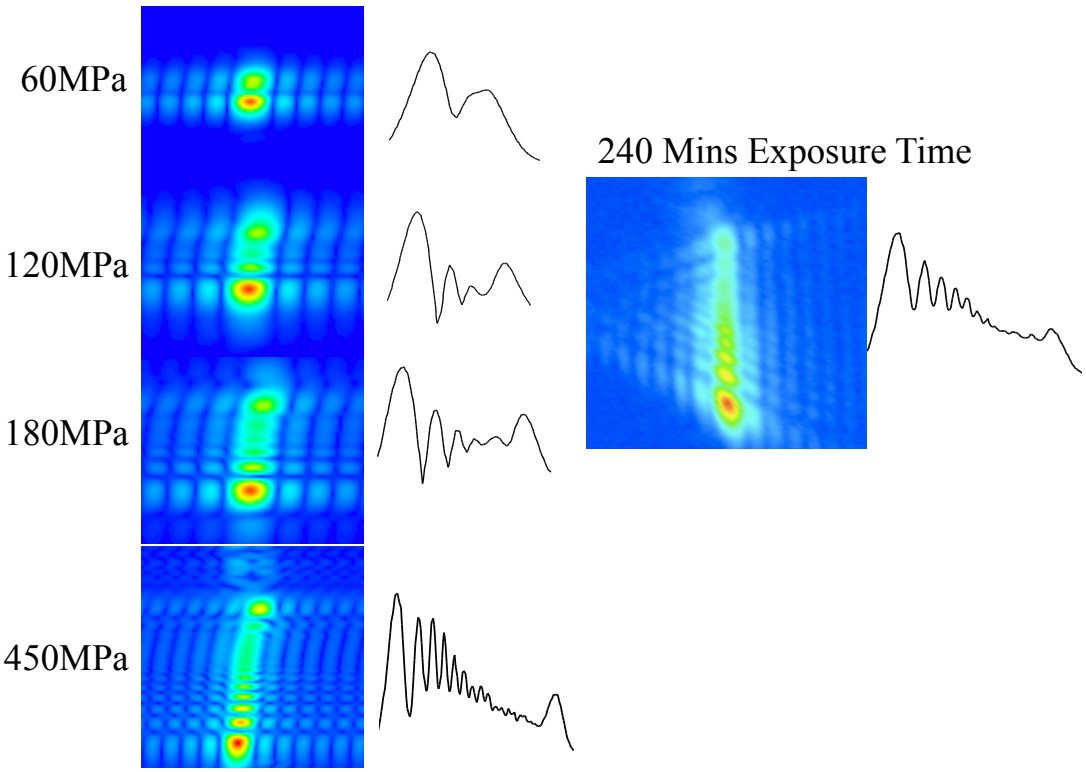

Fig. 22 Comparisons of simulated (left) and measured (right) diffraction patterns shown as 2D scalar-cut-plane and line plots.

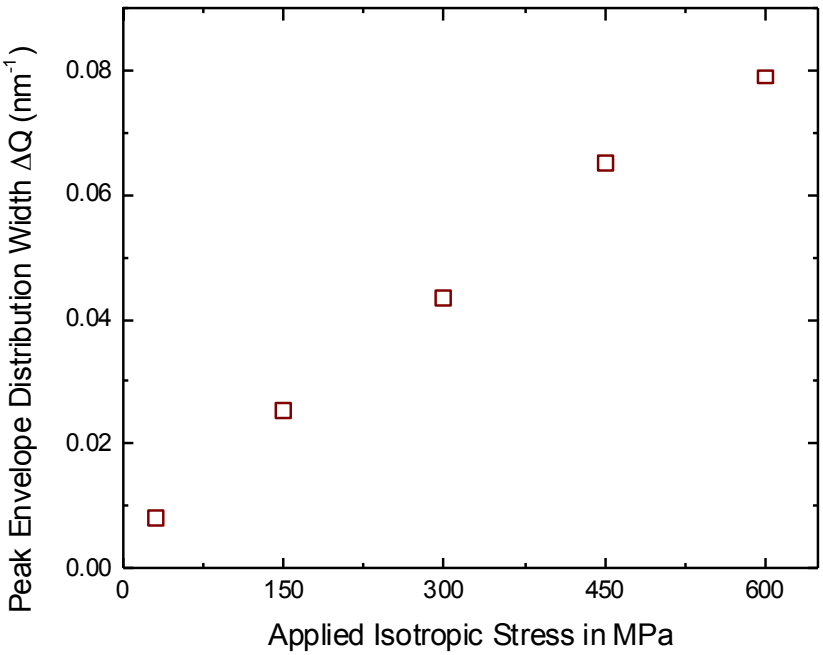

Fig. 23 Calculated widths of split-peak distributions (in reciprocal lattice units) of simulated diffraction patterns as a function of values of isotropic stress applied on the Silicon Dioxide layer.

Simulations with correct experimental conditions for measurements of radiation-induced bending of SOI nanowires were performed, The simulated SOI nanowire was rotated about 25 to 30 degree to match the real measurements with Si (111) Bragg peak orientation.

The features of the direct-space strains and amplitudes are maintained with the whole pattern rotated around 25 to 30 degree around y-axis in negative direction.

The corresponding diffraction pattern of the simulated object from COMSOL Multiphysics has about the same orientation of the experimental measured data.

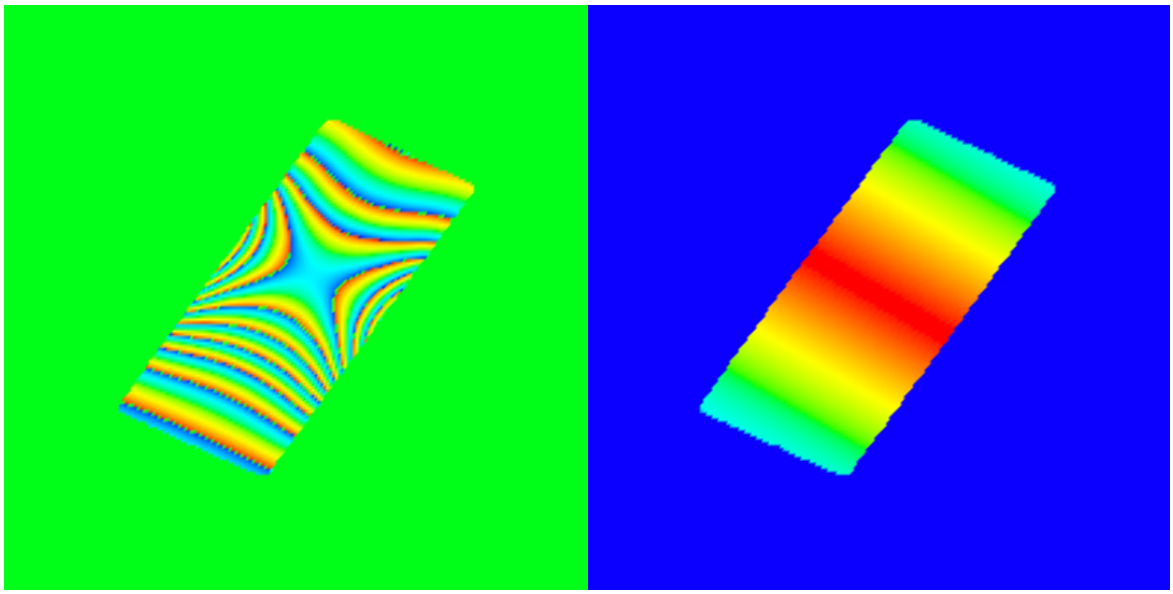

Fig. 24 Left: Scalar-cut-plane of phases of simulated direct-space SOI nanowire (FEA calculation is done by using COMSOL Multiphysics), Right: Amplitude of simulated SOI nanowire with introduction of a Gaussian probe function.

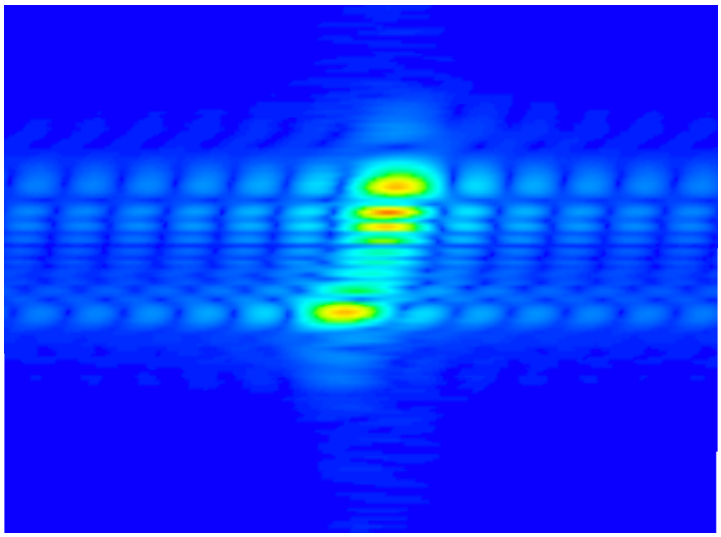

Fig. 25 Scalar-cut-plane of simulated diffraction pattern, which is DFT of Fig. 24

4:4 Simulations on highly strained twinned micro-crystals

Simulations of twinned micro-crystals with single, double or multiple phase-wraps are useful for understanding and analysing the origin of split-peaks in measured CDI diffraction patterns. Phase-wraps in both directions, i.e. both positive and negative phase gradients when reaching $+\pi / -\pi$ boundary are simulated so that comparisons of corresponding diffraction patterns can be done. Recent report shows extremely complex multi-peaks CDI measurements performed in Diamond I-16[56]; developments of effective iterative algorithms have been undergoing to understand and to successfully reconstruct such complicated diffraction patterns aiming at better understanding of structures; physical and chemical properties domains of twinned micro-crystals.

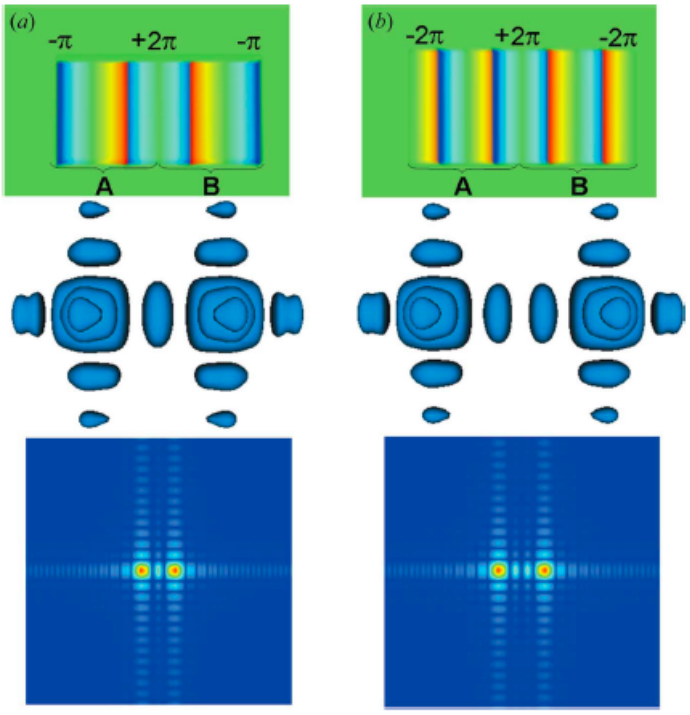

Fig. 26 (Top) Two bicrystals shown as a translucent three-dimensional box with colours representing the phase change. The two twins (A and B) have the same dimension (24 _ 24 _ 24 grid points) but different slopes of the phase ramps: (a) 1.5_, (b) 2_. (Middle) Calculated three-dimensional

coherent diffraction patterns of the two twinned objects. (Bottom) Isoscalar plane cut of the diffraction patterns[56].

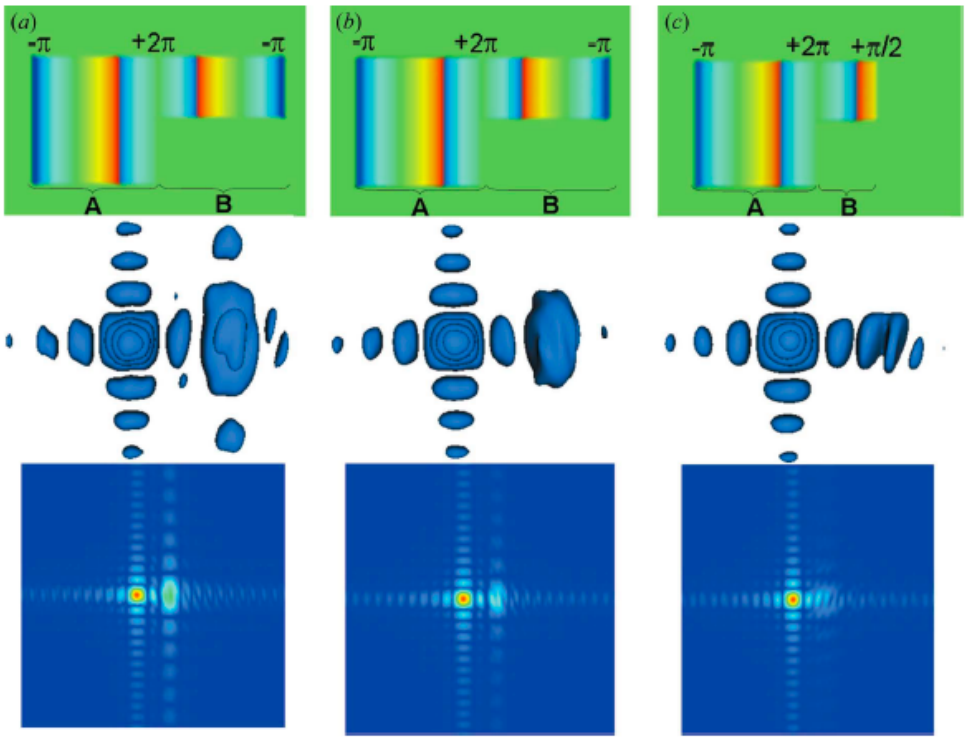

Fig. 27 (Top) Three bicrystals shown as a translucent three-dimensional box with colours representing the phase change. The two twins within each bicrystal have different dimensions: (a) (24 _ 24 _ 24) and (24 _ 12 _ 24), (b) (24 _ 24 _ 24) and (24 _ 12 _ 12) and (c) (24 _ 24 _ 24) and (12 _ 12 _ 12) grid points. (Middle) Calculated three-dimensional coherent diffraction patterns of the two twinned objects. (Bottom) Isoscalar plane cut of diffraction patterns[56].

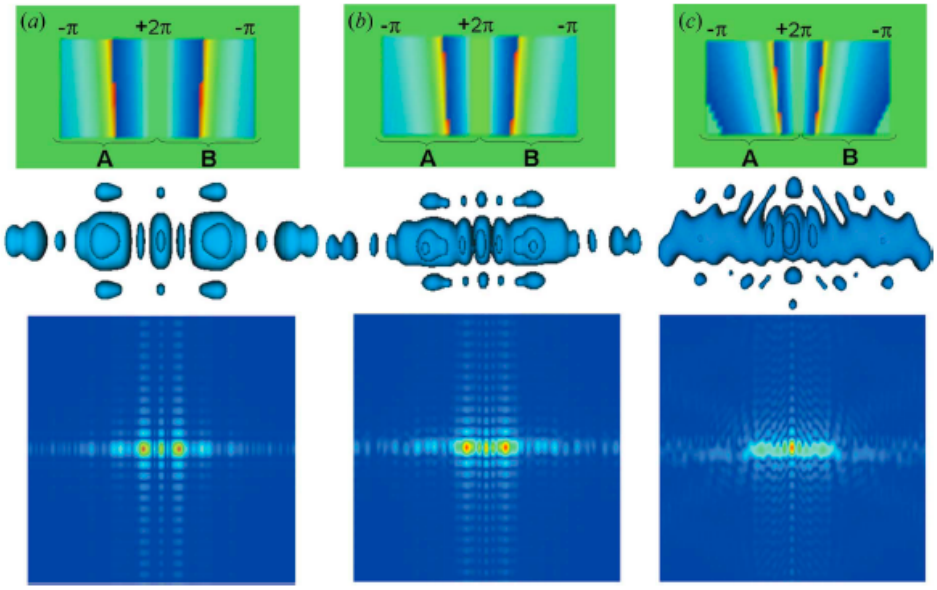

Fig. 28 (Top) Three bicrystals shown as a translucent three-dimensional box with colours representing the phase change. The two twins have the same dimension (24 _ 24 _ 24 grid points) and the same overall variation of the phase ramp. However, the curvature of the parabolic function changes in the three objects. The change has been modelled by displacing the minimum of the parabolic function by 78 (a), 35 (b) and 15 (c) pixels from the object. (Middle) Calculated three-dimensional coherent diffraction patterns of the twinned objects. (Bottom) Selected isoscalar plane cut for the diffraction patterns[56].

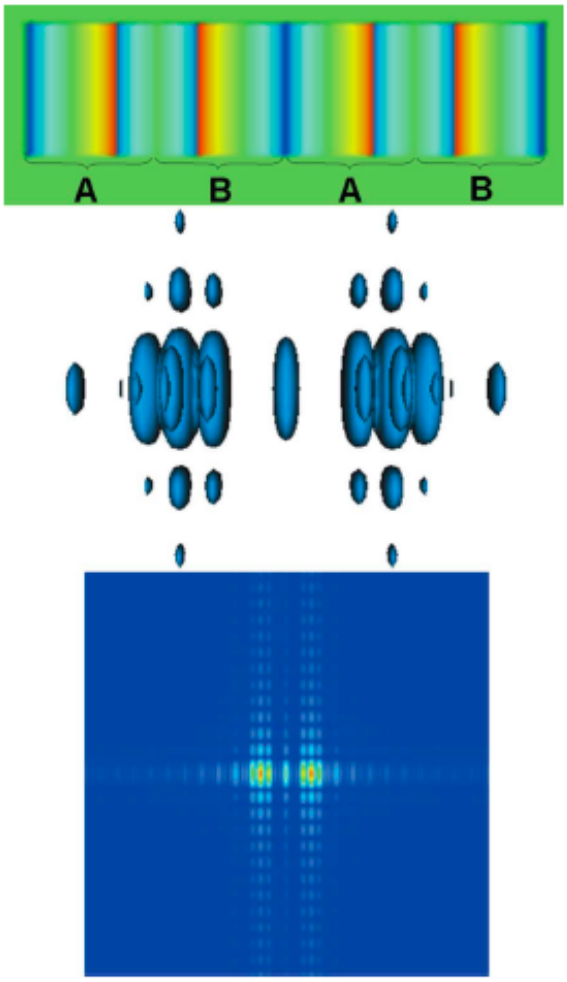

Fig. 29 (Top) Twinned crystal with four domains (ABAB) shown as a translucent three-dimensional box with the domain dimensions and phase ramps. (Middle) Calculated three-dimensional coherent diffraction pattern. (Bottom) Isoscalar plane cut of the diffraction pattern showing the speckles within the split peaks[56].

4:5 FEA Simulation of differential-strained Gold Nano crystals induced by thiol adsorption using COMSOL Multiphysics

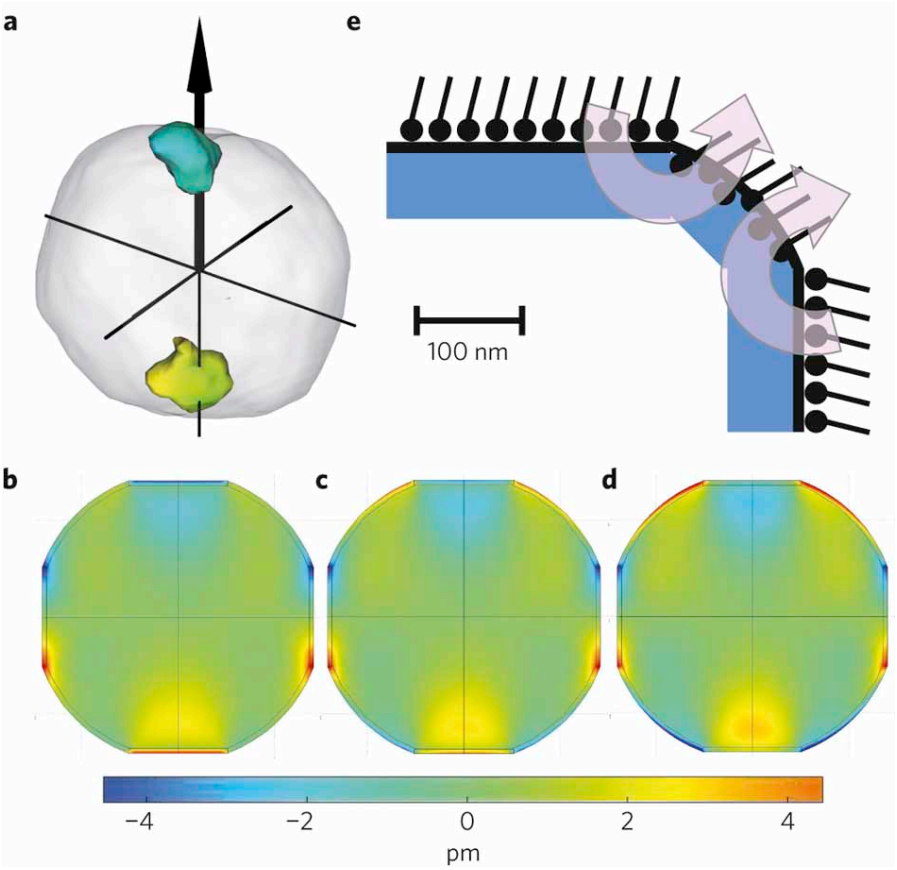

Fig. 30 a, Image of the measured crystal with a single contour of the difference density Δρ(r) superimposed, coloured according to its phase. b, Calculated vertical component of the displacements of a model facetted gold nanocrystal with a tensile surface stress σ_S=1.5 N m^{-1} applied to the facets alone. c, The same as in b with a tensile surface stress σ_S=0.75 N m^{-1} applied to the facets and a compressive surface stress σ_S=−0.75 N m^{-1} applied to the spherical surface regions. d, The same as in b with a compressive surface stress σ_S=−1.5 N m^{-1} applied to the spherical surface regions alone. A sphere of radius 145 nm is attached to a skin layer of 5 nm thickness used to apply the stress. Four 40° facets intercept the sphere, also with 5 nm skins. e, Schematic of the relative motions at the nanocrystal surface induced by thiol adsorption: the crystal's flat facets are observed to contract inwards relative to its spherical regions. Figure is from [6]

5. Conclusion and Future Outlooks

Our newly developed revised Hybrid-Input-Output Algorithm works in alternation with conventional Error-Reduction algorithm to improve data convergence of reconstructions of diffraction patterns of highly strained SOI nanowires due to radiation-induced bending. Simulations show that there are significant improvements on convergence of data reconstruction. Further developments have been made to utilize this algorithm to solve reconstructions of experimental data with highly strained features, and we plan to use our simulated model of direct-space amplitude phase values to direct reconstructions of data so that successful inversion are expected to be obtained. Our initial results give us some optimistic results and detailed studies have been undergoing to be reported in the near future.

We plan to measure strain patterns of SiGe nanowire and quantum dot based FET transistors by using nano-focused X-ray beam Bragg geometry ptychography technique at beamline 34-ID-C at APS. Coherent X-ray diffractive imaging (CDI) is a lensless technique in which an X-ray beam with high coherence properties is used to image a sample. The CDI method removes various aberration effects of a conventional lens-based system, it uses iterative algorithms to retrieve phase information lost during measurement, and is therefore sensitive to internal strains associated in nanostructure systems with phase-contrast imaging technique. It can provide us with shape information and quantitative strain measurements of the internal structures of single crystalline micro- and nanostructures. Combining conventional CDI with coherent scanning X-ray microscopy, i.e. ptychography with nano-focused beam studies enable us to directly extract structures of X-ray beam and our patterned SiGe nanowires within FET devices. Circular scans with nano-focused beam with around 100nm X 100nm focus spot should enable us to achieve appropriate degree of overlapping of the scanning patterns, thus reconstructions of two-dimensional amplitude and displacements of our Silicon-On-Insulator wires can be attempted, reconstruction of beam profile can be performed in the mean time. In the near future, we plan to develop algorithms that are suitable for reconstructions of three-dimensional Bragg-geometry ptychography studies on isolated

compact object.

A Silicon substrate is to be used which will have a different crystallographic orientation to that of the SiGe nanowires or quantum dots to be investigated. This allows the SiGe structures to be studied independent of interference from the substrate. Our SiGe nanowires and quantum dots are to be fabricated on commercial SiGe with (1,1,1) orientations of Silicon substrates and nanostructures by electron-beam lithography; reactive ion etching (RIE) and focused ion beam (FIB) techniques, all of which are to be done in our newly-installed facilities at London Centre for Nanotechnology based in London.

As a result of the different strain properties of structures at the nanoscale, SiGe nanowires and quantum dots are to be fabricated with various shapes and sizes. We envisage large strain field to be measured within active region of our lithographically fabricated state-of-art SiGe nanowire or quantum dot based FETs due to various fabrication and operation conditions. Therefore, in situ characterisations of our FET devices could be performed during Bragg ptychography measurements with various current-voltage features, and also with radiation and heating induced oxidation processes.

The experimental results of reconstructed strain patterns will be compared with the theoretical calculations that are to be performed using Finite-Element-Analysis package. We are confident that large-strained generated by our lithographically fabricated devices from commercial SiGe wafer (orientation of (111) handle) with nominal thickness of about 200nm are fully accessible with the current instrumentations at 34-ID-C at APS. Our current setups are ideal for carving devices of lateral dimension 30nm to 500nm to give structures with the ideal size for CXD. Although the signal from Si is relatively weak due to spatial dimensions, we have verified in previous experiments that our spatial resolution is as good as 0.07μm in all three dimensions, and we could certainly see SiGe nanowires or quantum dots up to 0.04 μm. SiGe alloy based nanowire/quantum dots FETs are reported to exhibit much better devices operating efficiency with much enhanced charge carriers' mobility. With employment of Bragg-geometry ptychography studies on these FETs devices, we expect to obtain quantitative strains results on temperature; oxidation and other device operation conditions with excellent accuracy of reconstructions, and currently no other equivalent methods could

compete with this particular technique at this level of resolution. Scanning Electron Microscopy, high Resolution Transmission Electron Microscopy and Atomic Force Microscopy are to be used as complementary methods to further confirm our experimental results in the later stage.

Our proposed sample preparation procedures involve RIE of Silicon and Gallium ion implantations with FIB methods. This doping procedure is likely to induce inhomogeneous strain patterns by diffusion of impurity ions into SiGe nanowire or quantum dot based FET devices. Strains will also be introduced as a result of a set of subsequent oxidation processes to be done during measurements at the APS. Furthermore, strains to be generated by reactive ion etching are to be compared so that the optimum etching parameters can be determined.

Reactive ion etching results in either straight or undercut sections of SiGe based FETs, We have tried with SF_6 gas and strong asymmetric reciprocal-space patterns were measured and analysed. With the help of our newly developed revised-fitting phase-constraint Hybrid-Input-Output algorithm, reconstructions of highly strained diffraction patterns were successful and we are in preparation to report our new results to be submitted soon. We plan to try Chlorine-based etching technique for the next run so that comparisons can be made to optimize our fabrication conditions.

We propose to perform circular scans with Fresnel circular zone-plate of focusing spot of around 100nm X 100nm, and appropriate guard and standard pinholes; slits will be placed before X-ray beam entering zone-plate. Appropriate diameter of zone-plate will be calculated with knowledge of both Longitudinal and transverse coherence length of X-ray at beamline 34-ID-C or other relevant beamlines at APS. Measurements on our individual SiGe nanowires and quantum dots within devices of dimensions of around 400μm X 400μm X 160nm, reconstructions of 50% to 70% degree of overlapping of two-dimensional Bragg diffraction patterns will be attempted. High-accuracy piezo-electric motor stage setup is required to accurately monitor the scanning positions in both dimensions of the plane perpendicular to the X-ray beam propagation direction. Reconstructions of density and phase of both the SOI crystal and probe will be studied by extended ptychographic iterative engine (ePIE). Suitable attenuation and beamstop will be used in this proposed experiment; both transmission and Bragg reflection geometries are to be employed. Our previous measurements on transmission

geometry have been analyzed and our reconstruction results have shown very useful information. Also, appropriate platus detector masks will be evaluated in the beginning of the proposed experiment to correct measurement data due to imperfection of pixels of our pilatus detector. The relatively small illumination volume of our proposed measurements and higher initial photon flux level; could enable us to use our pilatus detector of relatively large pixel size (170μm X 170μm). Recent developments at 34-ID-C enlarges the space available between diffractometer (where samples are placed) and pilatus detector, which means we are able to resolve much finer reciprocal space fringes with Pilatus detector at much larger distance from sample position.

It is recognized that semiconductor device carrier mobility can be substantially improved with applications of strain-technology, which is a crucial step for performance improvements in Silicon-based semiconductor devices. It has been found that strains induced in Silicon-based devices during fabrication processes can result in enhanced channel mobility[50]. Furthermore, it was reported that Silicon nanowires down to 10nm x 20nm cross-sections with doping are to exhibit substantial improvements of thermoelectric efficiency compared to bulk Silicon devices at various temperatures[57]. Band gaps of strained nano-sized semiconductors can be modified[51] and strained Silicon band gaps have been theoretically predicted to switch from indirect to direct[52]. This might advance device performance by the reduction of operating voltage to reduce the amount of heat dissipation across devices.

We hope scanning X-ray diffractive imaging technique (Bragg geometry ptychography)[58] is able to help us comprehend and acquire unique solution of our SOI nanostructures because of extra strong constraints in direct-space part of algorithm. Contribution of probe structure to the measured rocking curves can be a problem for extracting actual information solely to displacements and structures of SOI nanowires and micro-squares. With e-pie technique[59], we will be able to reconstruct both complex wave-functions of both probe and sample structures simultaneously to enable us to fully understand SOI nanostructures under various fabrication conditions, and ultimately evolution of strains within particular SOI deivces of industrial interests as a function of various devices operating parameters to maximize deivces performance, and to achieve the highest obtainable switching speed and efficiency.

Studies on atomic displacements of SOI nanostructures induced by Focused-Ion-Beam (FIB)

implantations into device structures are of great interest in semiconductors industry, and quantitative analysis of strain generation and relaxation are key to SOI and other semiconductor manufacturers. Our current CDI instrumentations allow us to see strains up to one lattice constant within crystalline structures with spatial resolution of around 30nm. We would be able to perform time-resolved strains evolution studies and mechanisms of FIB implantations could be understood systematically.

Ptychography[60] with circular scanning method should enable us to achieve appropriate degree of overlapping of the scanning patterns, thus reconstructions of two-dimensional amplitude and displacements of our Silicon-On-Insulator wires can be attempted, and reconstruction of beam profile can be performed in the mean time. Recently, some 2D and 3D Bragg geometry ptychography scans were obtained at beamline 34-ID-C at Advanced Photon Source, and currently, we are in the process of developing algorithms that are suitable for reconstructions of three-dimensional Bragg-geometry ptychography on crystalline structures. Some recent work of successful studies of three-dimensional Bragg ptychography on Silicon-On-Insulator structures were reported[48], relatively successful data recording and reconstructions were presented and the results have opened up potentially wider applications of surface sciences research on both compact and extended micro and nano-crystalline structures.

Ptychography and CDI results on SOI nanowire/micro-squares and SOI based MOSFET will be compared quantitatively aiming at good understanding of how strain and radiation affect device performance and lifetime, with excellent accuracy. This could in principle help current semiconductor industry to recognize the importance of device functionality as a function of strain and radiation effect, which is useful for fabrication and development of next generation Silicon-based MOSFET device to be implemented into commercial electronic industry. Recent studies on a single SiGe quantum dot embedded in functional Field Effect Transistor (FETs) by using X-ray nano-diffraction have shown some important results on strains within device[61], and this opens up a new research direction for characterization of nanowire based devices under operation conditions.

Studies on porous Silicon nanowires devices and SiGe core-shell nanowire-based NWFETs are to be performed in the near future for obtaining both quantitative and precise information on structural or morphological dependence on performances of various nanostructure semiconductor devices, which are crucial elements aiming at better understanding of the nature of Silicon nanostructure based devices with improved comprehension of quantum confinements in various dimensions. Recent studies show SiGe cylindrical core-shell nanowire based NWFETs demonstrate significant improvements on electron/hole charge carriers mobility and device efficiency[53]. We hope by using our novel Bragg CDI and two or three-dimensional pychography techniques, further studies could be vital for pinpointing underlying mechanisms that are responsible for these observed improvements. This may open a new path for direct-observation and in situ characterisation of nanostructure semiconductor devices ranging from sensors and optoelectronic devices.

Reference and Notes

1. Robinson, I. and R. Harder, *Coherent X-ray diffraction imaging of strain at the nanoscale.* Nature materials, 2009. **8**(4): p. 291-8.
2. Marcus C. Newton1, S.J.L., Ross Harder and Ian K. Robinson, *Three-dimensional imaging of strain in a single*

ZnO nanorod. Nature Materials, 2010. **9**: p. 120-124.

3. Harder, R., et al., *Imaging of complex density in silver nanocubes by coherent x-ray diffraction.* New Journal of Physics, 2010. **12**(3): p. 035019.
4. Favre-Nicolin, V., et al., *Coherent-diffraction imaging of single nanowires of diameter 95 nanometers.* Physical Review B, 2009. **79**(19): p. 195401.
5. Xiong, G., et al., *Elastic relaxation in an ultrathin strained silicon-on-insulator structure.* Applied Physics Letters, 2011. **99**(11): p. 114103.
6. Moyu Watari, R.A.M., Manuel Vögtli, Gabriel Aeppli, Yeong-Ah Soh,

Xiaowen Shi, Gang Xiong, Xiaojing Huang, Ross Harder and Ian K. Robinson, *Differential stress induced by thiol adsorption on facetted nanocrystals*. Nature Materials, 2011(10): p. 862–866.

7. Usuda, K., et al., *Strain characterization in SOI and strained-Si on SGOI MOSFET channel using nano-beam electron diffraction (NBD).* Materials Science and Engineering: B, 2005. **124-125**: p. 143-147.
8. Robinson, I., *Imaging matter in different spaces.* Physics, 2011. **4**.
9. Abbey, B., et al., *Keyhole coherent diffractive imaging.* Nature Physics, 2008. **4**(5): p. 394-398.
10. Minkevich, A.A., et al., *Strain field in (Ga,Mn)As/GaAs periodic wires revealed by coherent X-ray diffraction.* EPL (Europhysics Letters), 2011. **94**(6): p. 66001.
11. FRIEDEL, G. (1913). C. R. Acad. Sci., _Paris, 187, 1533.
12. Pfeifer, M.A., et al., *Three-dimensional mapping of a deformation field inside a nanocrystal.* Nature, 2006. **442**(7098): p. 63-6.
13. Williams, G.J., *Microscopy of Au Microcrystals by Coherent X-Ray Diffractive Imaging*. PhD thesis, 2004.
14. Steven J. Leake, M.C.N., Ross Harder and Ian K. Robinson, *Longitudinal coherence function in X-ray imaging of crystals.* OPTICS EXPRESS, 2009. **17**(18): p. 15853-15859.
15. Jesse N. Clark, R.H., Xiaojing Huang and Ian K. Robinson, *X-ray Diffraction Imaging with Partial Coherence*. Summited to Nature Photonics, 2011.
16. Nugent, K.A., *Coherent methods in the X-ray sciences.* Advances in Physics, 2010. **59**(1): p. 1-99.
17. Vartanyants, I., et al., *Coherence Properties of Individual Femtosecond Pulses of an X-Ray Free-Electron Laser.* Physical Review Letters, 2011. **107**(14).
18. From lecture notes from Dissemination of IT for the Promotion of Materials Science (DoITPoMS), University of Cambridge, http://www.doitpoms.ac.uk/
19. Robinson, I. and R. Harder, *Coherent X-ray diffraction imaging of strain at the nanoscale.* Nat Mater, 2009. **8**(4): p. 291-8.
20. X-RAY DATA BOOKLET, Center for X-ray Optics and Advanced Light Source Lawrence Berkeley National Laboratory
21. X-RAY DATA BOOKLET, Center for X-ray Optics and Advanced Light Source Lawrence Berkeley National Laboratory

22. Elements of Modern X-ray Physics, By Jens Als-Nielsen and Des McMorrow, John Wiley & Sons, Ltd.
23. Optical Physics, 4th edition, By Ariel Lipson, Stephen G. Lipson, Henry Lipson, Cambridge University Press.
24. C. Scheringer, X-ray Bragg scattering in the Born-Oppenheimer approximation, Acta Cryst. (1979). A35, 340-342
25. C. Scheringer, X-ray Bragg scattering in the Born-Oppenheimer approximation. II, Acta Cryst. (1980). A36, 497-499
26. Huang, X., et al., *Propagation uniqueness in three-dimensional coherent diffractive imaging.* Physical Review B, 2011. **83**(22).
27. Newton, M., et al., *Phase retrieval of diffraction from highly strained crystals.* Physical Review B, 2010. **82**(16).
28. RODENBURG, J.M., *THE PHASE PROBLEM, MICRODIFFRACTION AND WAVELENGTH-LIMITED RESOLUTION - A DISCUSSION.* Ultramicroscopy, 1989. **27**: p. 413-422.
29. J. Miao, J.K.a.D.S., *The oversampling phasing method.* Acta Crystallographica Section D; Biological Crystallography, 2000. **D56**: p. 1312-1315.
30. D., S., *Some implications of a theorem due to Shannon.* Acta Cryst., 1952. **5**: p. 843.
31. Song, C., et al., *Phase retrieval from exactly oversampled diffraction intensity through deconvolution.* Physical Review B, 2007. **75**(1).
32. Thibault, P., et al., *High-resolution scanning x-ray diffraction microscopy.* Science, 2008. **321**(5887): p. 379-82.
33. Dierolf, M., et al., *Ptychographic X-ray computed tomography at the nanoscale.* Nature, 2010. **467**(7314): p. 436-9.
34. Tripathi, A., et al., *Dichroic coherent diffractive imaging.* Proc Natl Acad Sci U S A, 2011. **108**(33): p. 13393-8.
35. Dierolf, M., et al., *Ptychographic coherent diffractive imaging of weakly scattering specimens.* New Journal of Physics, 2010. **12**(3): p. 035017.
36. Berenguer de la Cuesta, F., et al., *Coherent X-ray diffraction from collagenous soft tissues.* Proc Natl Acad Sci U S A, 2009. **106**(36): p. 15297-301.
37. Godard, P., et al., *Three-dimensional high-resolution quantitative microscopy of extended crystals.* Nat Commun, 2011. **2**: p. 568.

38. Unpublished work done by Bean et al, London Centre for Nanotechnology, University College London, U.K.
39. Henry, M.D., Shearn, M. J., Chhim, B., Scherer, A., *Ga+beam lithography for nanoscale silicon reactive ion etching.* Nanotechnology, 2010. **21**(24): p. 245303.
40. Drake, T.S., M.L. Lee, A.J. Pitera,. E.A. Fitzgerald, D.H. Anjum, J. Li, N.K. R. Hull, and J.L. Hoyt, , *Fabrication of Ultra-Thin Strained Silicon on Insulator.* Journal of Electronic Materials, 2003. **32**(9): p. 972-975.
41. Jaju, V., *Silicon-On-Insulator Technology*, in *Advances in MOSFETs EE530*2004.
42. Fujioka, H., *Method of manufacturing semiconductor on insulator*, U.S. Patent, Editor 1991.
43. Bich-Yen Nguyen, G.C., and Carlos Mazuré, *A Review of SOI Technology and its Applications.* Journal Integrated Circuits and Systems, 2009. **4**(2): p. 51-54.
44. B. Aspar, M.B., H. Moriceau, C. Maleville, T. Poumeyrol, A.M. Papon, *Basic mechanisms involved in the Smart-Cut process.* Microelectronic Engineering, 1997. **36**(1-4): p. 233-240.
45. Shi, X., et al., *Structural inhomogeneity in silicon-on-insulator probed with coherent X-ray diffraction.* Zeitschrift für Kristallographie, 2010. **225**(12): p. 610-615.
46. Cha, W., et al., *Exploration of crystal strains using coherent x-ray diffraction.* New Journal of Physics, 2010. **12**(3): p. 035022.
47. Loren Beitra, M.W., Takashi Matsuura, Naonobu Shimamoto Ross Harder and Ian Robinson, *Confocal Microscope Alignment of Nanocrystals for Coherent Diffraction Imaging.* AIP Conference Proceedings, 2010. **CP1234**: p. 57-60.
48. Godard, P., et al., *Three-dimensional high-resolution quantitative microscopy of extended crystals.* Nature communications, 2011. **2**: p. 568.
49. Polvino, S.M., et al., *Synchrotron microbeam x-ray radiation damage in semiconductor layers.* Applied Physics Letters, 2008. **92**(22): p. 224105.
50. Ieong, M., et al., *Silicon device scaling to the sub-10-nm regime.* Science, 2004. **306**(5704): p. 2057-60.
51. Ki-Ha Hong, J.K., Sung-Hoon Lee, and Jai Kwang Shin, *Strain-Driven Electronic Band Structure Modulation of Si Nanowires.* Nano letters, 2008. **8**(5): p. 6.
52. Zhao, X., et al., *Quantum Confinement and Electronic Properties of Silicon Nanowires.* Physical Review Letters, 2004. **92**(23): p. 236805.
53. Xiang, J., et al., *Ge/Si nanowire heterostructures as high-performance field-*

effect transistors. Nature, 2006. **441**(7092): p. 489-493.

54. Wackerman, J.R.F.a.C.C., *Phase-retrieval stagnation problems and solutions*. Optical Society of America, 1986. **3**(11): p. 1897-1907.
55. Fienup, J.R., *Phase retrieval algorithms-a comparison*. APPLIED OPTICS, 1982. **21**(15): p. 2758-2769.
56. Aranda, M.A., et al., *Coherent X-ray diffraction investigation of twinned microcrystals*. J Synchrotron Radiat, 2010. **17**(6): p. 751-60.
57. Boukai, A.I., et al., *Silicon nanowires as efficient thermoelectric materials*. Nature, 2008. **451**(7175): p. 168-171.
58. Berenguer de la Cuesta, F., et al., *Coherent X-ray diffraction from collagenous soft tissues*. Proceedings of the National Academy of Sciences, 2009. **106**(36): p. 15297-15301.
59. Maiden, A.M. and J.M. Rodenburg, *An improved ptychographical phase retrieval algorithm for diffractive imaging*. Ultramicroscopy, 2009. **109**(10): p. 1256-62.
60. Rodenburg, J., et al., *Hard-X-Ray Lensless Imaging of Extended Objects*. Physical Review Letters, 2007. **98**(3).
61. Hrauda, N., et al., *X-ray nanodiffraction on a single SiGe quantum dot inside a functioning field-effect transistor*. Nano letters, 2011. **11**(7): p. 2875-80.

Timetable for Completion of PhD Thesis

Xiaowen Shi

Apr-May 2012	Reconstruction work on highly strained SOI nanowires
June-July 2012	Two-week experiments at Advanced Photon Source (Bragg Ptychography on SOI wafers; less-strained SOI structures (Work with Maria) and Bragg CDI on GeSi and SSOI (Work with Gang) **Wilhelm and Else Heraeus Physics School** *"Microelectronics for Society – More than Moore expands More Moore" in Germany* Guided-phase coherent diffraction imaging of strongly bent Silicon nanowires Xiaowen Shi, Gang Xiong, Xiaojing Huang, Jesse Clark, Ross Harder and Ian Robinson, to be submitted to Physical Review Letters (2012) Start Final PhD thesis
Aug- End of Oct 2012	XRM Conference, Shanghai, P.R. China Finish First version of PhD thesis
Mid-Nov 2012	Submit Final PhD thesis

Dec 2012/Jan 2013	PhD Viva